PHASE LOCKING IN FIBER LASER ARRAYS

by

FANTING KONG

A dissertation submitted to the Graduate Faculty in Physics in partial fulfillment of the requirements for the degree of Doctor of Philosophy, The City University of New York

2010

This manuscript has been read and accepted for the
Graduate Faculty in Physics in satisfaction of the
dissertation requirement for the degree of Doctor of Philosophy.

Professor Ying-Chih Chen

Date — Chair of Examining Committee

Professor Steven Greenbaum

Date — Executive Officer

Doctor Ronald H. Silverman

Professor Kai Shum

Professor Yuhang Ren

Professor Hyungsik Lim

Supervisory Committee

THE CITY UNIVERSITY OF NEW YORK

Abstract

PHASE LOCKING IN FIBER LASER ARRAYS

by

Fanting Kong

Adviser: Professor Ying-Chih Chen

This dissertation reports a series of studies on phase locking in two-element laser arrays, with an emphasis on fiber laser arrays, and an application of Q-switched microchip laser to high-resolution photoacoustic imaging. Phase locking is achieved by coupling the lasing elements to a common Fourier-transform resonator, in which the lasing elements and the output mirror are positioned in the focal planes of a converging lens so that the far-field profiles of the laser elements are projected to the output mirror through Fourier transformation. Since the far-field profiles generally have simpler and more symmetric structures, the relative phase of the lasing elements can be selected by placing a simple spatial filter on the output mirror. We have studied phase locking in fiber lasers operating in the continuous-wave mode and in stimulated-Brillouin-scattering (SBS) Q-switched mode, and in Q-switched microchip laser arrays formed in a single crystal. These systems represent vastly different parameters which can affect the development of phase locking. We have found that the continuous-wave fiber lasers can always be phase locked and the relative phase remains stable despite random phase fluctuations in individual fibers. This is attributed to the combination of broad bandwidths of the

fiber gain media and small frequency spacing of the longitudinal mode which allows resonance frequencies of the composite resonator of the laser array to be found under all circumstances. In short-pulse laser arrays, phase locking can be realized only when the fiber lengths are nearly equal in the SBS Q-switched fiber lasers, or the frequency mismatch is less than the bandwidth of the laser pulse in the microchip laser array. In the latter case, the boundary of phase-locked and unlocked states is characterized by partial coherence in the combined laser beam due to the pulses from the individual elements not perfectly overlapping in time.

Photoacoustic images are constructed based on the ultrasound signals generated when a tissue undergoes thermal expansion after laser pulses are absorbed by chromophores in the tissue. The use of focused laser pulse and high-frequency ultrasound has led to much higher image resolution than obtainable with conventional pulse-echo ultrasound. The ability to identify chemical compositions in tissues based on their distinct wavelength-dependent optical absorption also leads to new capabilities in diagnostic imaging.

ACKNOWLEDGEMENTS

I can not imagine that I could come so far without the generous and endless assistance of many people. It is my privilege to express my gratitude to them for helping me these years.

First, I would like to thank my PhD advisor, Professor Ying-Chih Chen, for being a great mentor, guide and supporter. His passionate and persistent attitude toward the research had inspired and motivated me in my work and life. His patience and understanding of my circumstances help me through many challenges to get to this step.

I am heartily thankful to Dr. Ronald H. Silverman, whose encouragement and guidance from the initial to the final level enable me to develop an understanding of a new subject. His deep knowledge helps me through many difficulties that I encountered.

I am grateful to all my teachers during my each stage. Their warm encouragement and guidance and illuminative educations are unforgettable in my heart.

I would like to thank Richard Krumm, our laboratory technician, for many finished experimental parts he makes, which gives me a lot of help.

I am also indebted to many of my collaborators: Liping Liu, Harriet O. Lloyd and Yi Zhou, who support me with good suggestions, preparing the samples and sharing the experience with me. Special thanks to the Graduate Center and Hunter College of the City University of New York for supporting me to complete my studying here. I also would like to thank all the faculties and staffs in the Physics and Astronomy Department at Hunter College, their warm hearts give me a good time here.

Finally, I want to express my deepest gratitude to my parents and wife, especially my father. You give me the hope and support that take me through all the difficulties in my life. None of my work could be completed without your endless love and patience.

Table of Contents

List of Illustrations

Figure

Chapter 1

Introduction

The maximum output power of single-element lasers, such as diode lasers and fiber lasers, is limited by the power density of optical damage and nonlinear optical effects. For example, short pulses of 2 – 5 ns duration and several microjoules of pulse energy have been demonstrated in fiber lasers [1-4]. For such narrow pulses, the peak power of the laser in the core of the fiber is on the order of GW/cm^2 which is comparable to or exceeding the optical damage threshold of 20 GW/cm^2 in silica fibers. The power density of short pulses generated by stimulated Brillouin scattering in our laboratory exceeds 18.8 GW/cm^2 and has indeed caused occasional damage in fiber ends. To extend the upper limit of the output power, combining the output of multiple lasers is the logical next step.

Coherent operation of a one-dimensional laser array containing N equally-spaced elements can result in a peak power that is proportional to N^2 in the far field and a beam divergence proportional to N^{-1}, provided that all the elements in the array have the same phase. However, making all the elements in a laser array operate in the same phase is a challenging task. Each laser is a nonlinear oscillator and interacts with other oscillators in the array in a complex way. A laser array containing N elements has N supermodes, each having a distinct relative phase between adjacent elements. The most desirable supermode is the fundamental mode with all the elements operating in the same phase and interfering constructively in the forward direction.

However, the mode that has the highest gain is not necessarily the fundamental mode. Some form of mode control mechanism is needed to select the desirable mode. Even if all the elements are phase locked at a given time, the relative phase can be disrupted when the system is subjected to mechanical and thermal effects. For example, a temperature increase of 0.01 C can cause a phase change of 1π in a 5-meter-long glass fiber due to thermal expansion and thermally-induced refractive index change in glass and a phase change of π can totally alter the interference condition. Thus the phase locking mechanism must be able to adapt to the ever changing phase in optical fibers.

1.1 Phase locking methods

Various schemes of coupling multiple continuous-wave (CW) or quasi-CW fiber lasers in a coherent manner have been reported recently. A well-studied example is the Talbot resonator, which utilizes the self-imaging property of coherent periodical structure in the near field [5]. Exact replicas of the light emitters are formed periodically after certain distances of propagation in free space. These distances are an integer multiples of the Talbot distance given by $Z_t = \frac{2d^2}{\lambda}$,where λ is the free-space wavelength and d is the separation of the periodic light emitters. The image patterns for the in-phase and out-of-phase modes at the Talbot planes and fractional Talbot planes, which are located at ¼ and ½ of the Talbot distance, are illustrated in Fig. 1.

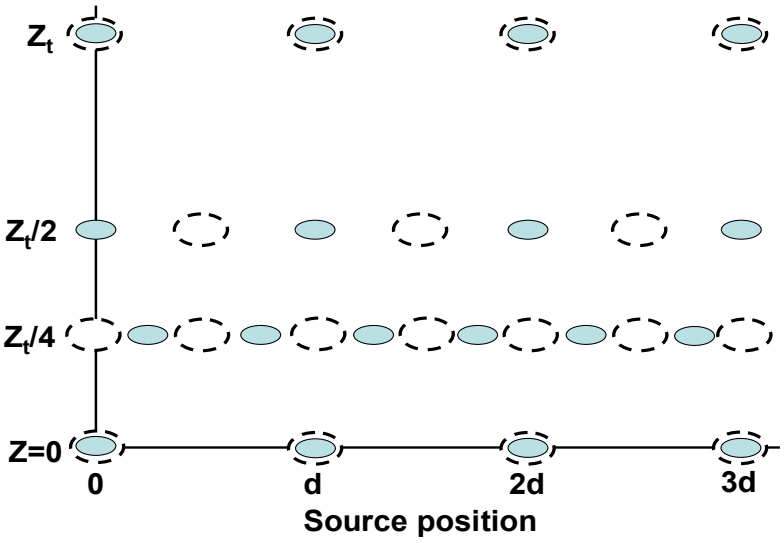

Figure1. Image patterns at the Talbot and fractional Talbot planes [5]

In Fig.1 the dashed and solid ovals correspond to the bright spots of the in-phase and the out-of-phase transverse mode, respectively. These Talbot images are the interference fringes where the waves from multiple emitters overlap in the near field. A mirror placed at $\frac{Z_t}{8}$ can reflect the image of the in-phase mode back to the light emitters to facilitate the coupling. This is the general idea of the linear (1-D or 2-D) Talbot cavity. The Talbot resonator works well in systems with a large number of elements where the distortion of wavefronts near the edges is negligible.

A similar self-imaging effect also exists in annular periodic structures, although the annual Talbot image is never an exact replica of the light source. Because the annular Talbot image is not an exact replica of the light source, the feedback efficiency is generally low as reported by M. Wrage [6,7]. Since the Talbot effect is a diffraction phenomenon in the near field, the

diffraction patterns are generally complex and the alignment is difficult. Also the Talbot resonator tends to favor the out-of-phase mode, which is not desirable, and has never resulted in the single-mode operation with diffraction-limited performance.

Another method to facilitate phase-locking is using the self-Fourier cavity, first reported by Corcoren et al. [8]. The self-Fourier cavity, as illustrated in Fig. 2 for a seven-element laser array, utilizes the property that the Fourier transform of the electric field of a periodic light source with a Gaussian envelop can reproduce the electric field of the light source itself under appropriate conditions.

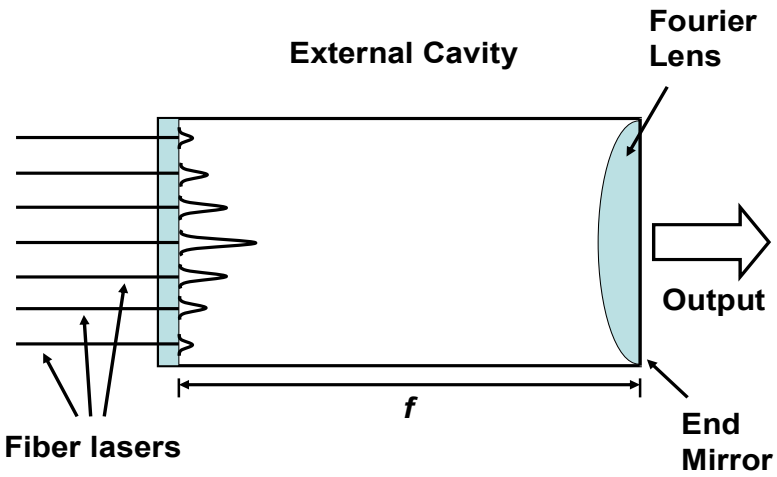

Figure 2. Self-Fourier laser cavity [8]

As shown in Fig. 2, the electric field of the seven-element laser array with a Gaussian envelop can be described by: $E(x) = \sum_{n=-\infty}^{+\infty} \exp\left\{-\left[\frac{(x-nb)}{a}\right]^2\right\} \exp\left[-\left(\frac{nb}{c}\right)^2\right]$, where parameter a represents the $1/e^2$ width of each element, b is the center-to-center spacing between the elements,

and c is the $1/e^2$ width of a Gaussian envelope distribution. When the laser array is placed at the focal point of a converging mirror, the Fourier transform of the light source is formed at the same plane as the light source. By requiring the Fourier transform of the light source reproduce the light source itself, the condition is found to be $b^2 = f\lambda$. This configuration favors the radiation pattern of the in-phase mode which has the highest feedback efficiency. Thus this approach has a self-filtering mechanism for the in-phase mode. The disadvantage of this method is that the intensities of each individual fiber lasers are not the same, with the fiber lasers near the edges having lower power than those in the middle. Thus at a high pumping level, the gain of the fiber lasers near the edges are higher than those near the center because the stored energy is not depleted. The higher undepleted gain near the edges tends to promote the higher-order modes.

Another method, first demonstrated by Cheo et al. is to use the multicore configuration in which multiple cores in an annular formation embedded in a common cladding are phase locked in the in-phase mode through the evanescent coupling [9]. The approach of Cheo cannot be scaled up to include a large number of elements without losing the efficiency and the ability to maintain a single transverse mode.

Wickham, et al. reported an active phase correction technique in four-element fiber array [10]. The approach involves interferometric detection of the phase deviation of each laser element from that of a reference beam and adjustment of the phase error in each element through individual phase modulators. This technique requires complicated setups for interferometric detection and phase adjustment in each element and may not be suitable for laser arrays with a large number of elements.

1.2 Phase locking with Fourier transform resonator

For my dissertation, I have been working on the problem of phase locking of laser arrays in one- and two-dimensional formations. The approach is to couple all the elements in a laser array to a common Fourier transform resonator which allows the phase control of the laser array to be done in the far field where the beam profiles are relatively simple. The schematic of the Fourier transform resonator is shown in Fig. 3. [11] Let $f(x,y)$ be the complex electric field of the optical wave emitted by the laser array which is placed at the front focal plane M1. After the wave propagates through free space and the converging lens, the electric field of the output wave at the other focal plane M2 is $g(x,y) = h_l \times F\left(\frac{x}{\lambda f}, \frac{y}{\lambda f}\right)$, where $F(v_x, v_y) = \int_{-\infty}^{\infty}\int f(x,y)\exp[j2\pi(v_x x + v_y y)]dxdy$ is the Fourier transform of $f(x,y)$ with spatial frequencies: $v_x = \frac{x}{\lambda f}$, $v_y = \frac{y}{\lambda f}$ and $h_l = (j/\lambda f)\exp(-j2kf)$.

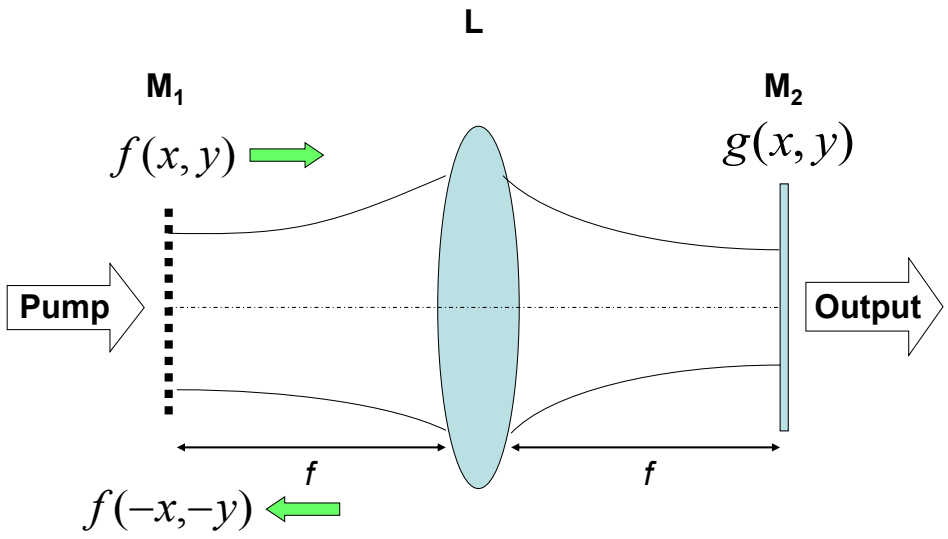

Figure.3 Schematic of a Fourier transform resonator.

If an output mirror is placed at plane M2, the wave is partially reflected. After passing through the converging lens, the electric field of the wave arriving at focal plane M1 would be $f(-x,-y)$, which is the Fourier transform of *g(x, y)*. For a field distribution $f(x,y)$ with inversion symmetry in the x,y plane, the field distribution of the reflected wave at M1 is the same as that of the input wave, resulting in a coupling efficiency of 1. In this configuration, the field pattern at plane M2 is the far field pattern of that at M1. The advantage of dealing with the far-field pattern is that the beam profile in the far field is much simpler than that in the near field. When all the elements are operated in the same phase, the far field pattern at plane M_2 would be a single-lobed Gaussian-like profile and the in-phase mode of the system can be selected by placing a simple spatial filter on the output mirror at M_2 that selectively reflects the in-phase mode,

Fig. 4 shows the calculated and observed beam profiles for various supermodes of a 2x2 laser array [12]. For the 2x2 laser array with a near field profile shown in Fig 4(a), the corresponding far-field beam profiles are shown in Fig. 4(b) for the in-phase mode and in Figs. 4(c) an 4(d) for phase differences of $\Delta\phi = \frac{\pi}{2}, \frac{3\pi}{2}$ and $\Delta\phi = \pi$ respectively. The dotted lines in Figs. 4(b) and 4(d) illustrate how a spatial filter composed of thin wires placed along the dark fringes of the in-phase mode can cause a higher loss to the out-of-phase mode without affecting the in-phase mode.

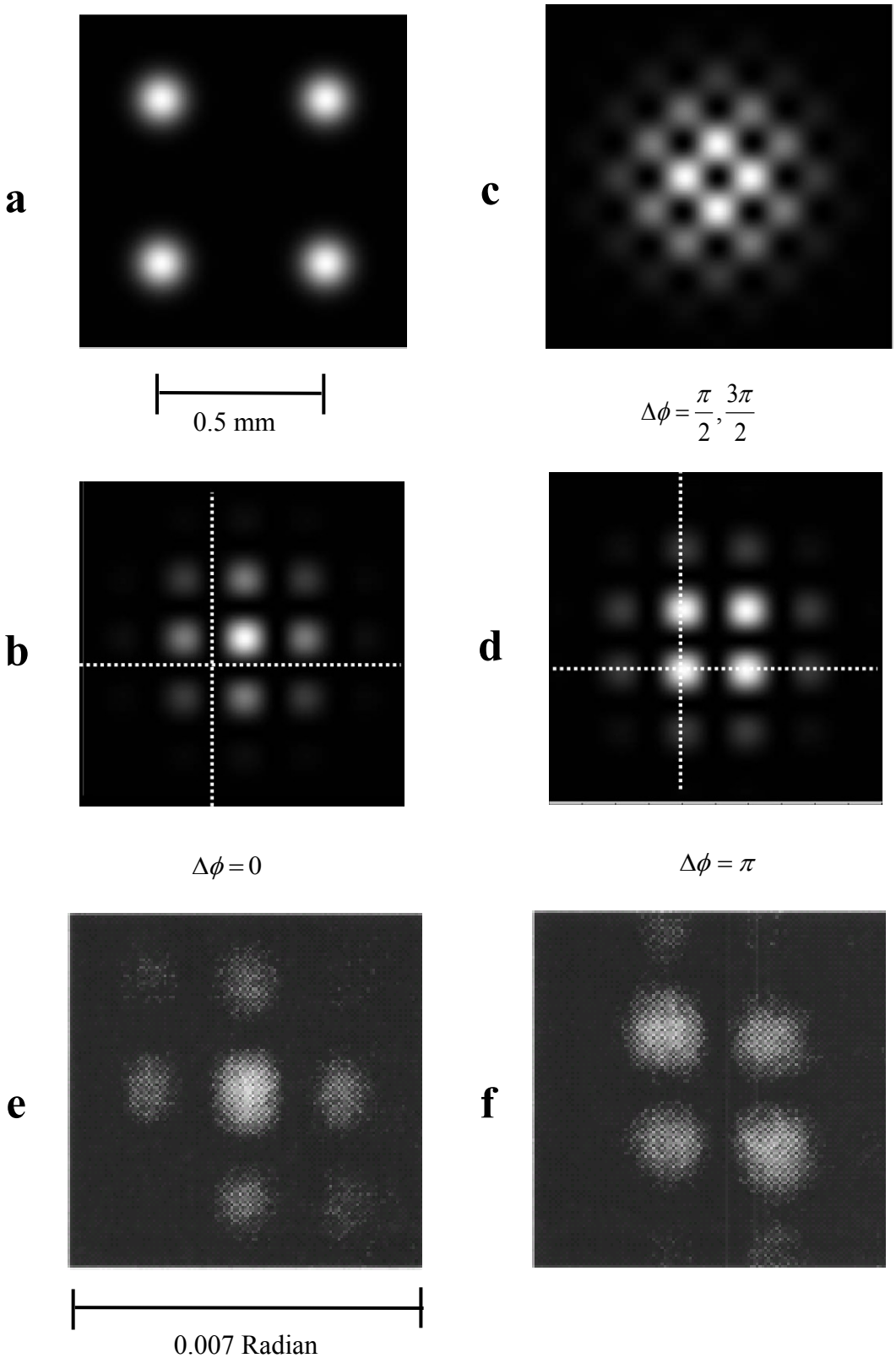

Figure 4: Calculated beam profiles: a) at the emitters, and b), c), d) in the far field, and observed far-field beam profiles for e) in-phase and f) out-of-phase modes.[12]

Our laboratory has recently demonstrated the phase-locked operation of a 2x2 Nd:YAG laser array using the Fourier resonator. Figs. 4(e) and 4(f) show the observed far-field beam profile in the in-phase and out-of-phase modes, respectively.

1.3 Outline

This dissertation is organized as follows: Chapter two is dedicated to phase locking in a two-element Ytterbium (Yb) doped fiber laser array in a common Fourier transform resonator containing a spatial filter. We have demonstrated that, despite the constant and random changes in the optical path lengths of the individual fibers, stable phase locking between fiber lasers can be maintained when the fiber lasers are coupled to a common resonator [11]. The ability to adapt to the changing environment is attributed to a self-adjusting process that can take place only in systems with a combination of long cavity length, broad gain bandwidth, and low Q resonator, all of which can be found in the Yb doped fiber lasers.

Chapter three is devoted to phase-locked Q-switched pulse generation in a two-element fiber laser array through stimulated Brillouin Scattering (SBS). The SBS pulse generated in fiber laser has a pulse duration of 1.5 ns which is much shorter than the 100-ns transit time for the pulse traveling in the laser cavity [14]. Despite the stochastic dynamics of nonlinear pulse generation and short pulse duration compared with the laser traveling time in the cavity, simultaneous generation of phase-locked short pulses has been achieved by combining diffractive coupling and spatial filtering in a Fourier transform resonator.

Also, the effects of frequency mismatch between the elements on phase locking have been studied using a system of two microchip lasers created on a single chip. The device parameters in

this system are opposite extremes from those of the fiber lasers in term of cavity length, bandwidth, and resonator Q-values. We have found that stable phase locking of 5-ns pulses with a high degree of spatial coherence can be obtained when the frequency mismatch is less than the spectral linewidth of the laser pulses [15]. As the frequency mismatch increases, the transition from the phase locked to unlocked states is characterized by gradual loss of temporal overlap of the pulses and a reduction in the fringe contrast of the combined beam due to loss of spatial coherence.

Chapter four is devoted to a totally different subject, namely an application of short-pulse solid-state lasers to high-resolution photoacoustic imaging which I have been working on since 2008 when an opportunity presented itself [16]. In conventional ultrasound imaging, a short ultrasound pulse is emitted by a transducer and reflections or echoes are generated whenever the ultrasound encountered a change in tissue density. The arrival time of the echo tells the locations of the reflections. In photoacoustic imaging, an intense short light pulse is directed at a tissue and the energy deposited in the tissue due to optical absorption causes a slight temperature increase. The thermal expansion of the tissues generates an ultrasound signal, which is a pressure wave and in turn is detected by a transducer. The arrival time of the signal tells the location of ultrasound source. The combination of light and sound in imaging has led to much higher image resolution and new capabilities that are not available when the imaging was done with light or sound alone. Promising preliminary results will be described.

Chapter 2

Phase locking in Continuous Wave (CW) and Quasi-CW Fiber laser Arrays

Rare-earth-doped fiber lasers are becoming the geometry of choice for high-power solid-state lasers because of proven advantages in compactness, efficiency, mechanical and thermal stability and beam quality. To date, a-single mode fiber laser producing an output of kilowatts has been demonstrated. [17] The ultimate limitation of output power from a single fiber laser is limited by optical damage and the onset of nonlinear effects such as stimulated Raman scattering and stimulated Brillouin scattering. Further increase in output power will require coherent addition of the outputs from multiple lasers in a laser array. In fiber lasers, due to the random and constant varying indices of refraction of the fibers, maintaining a constant phase among the lasing elements was thought to be a challenge. This Chapter reports our work on phase locking in two Ytterbium (Yb)-doped fiber laser array coupled to a common external Fourier resonator containing a spatial filter. We have found that despite the constant and random phase fluctuations in individual fibers, stable relative phase between the two fibers can be maintained. The ability to adapt to the changing phase is attributed to a self-adjusting process that can take place only in systems with a combination of long cavity length, broad gain bandwidth, and low Q resonator, all of which can be found in fiber lasers. [11]

2.1 Ytterbium doped fiber laser

As one of the most versatile laser ion, ytterbium (Yb) has several very attractive features. Firstly, it has a broad absorption band from below 850nm to above 1070nm which is shown in Fig. 5 [18]. Yb-doped fiber laser thus can be pumped with a wide selection of diode lasers at different wavelengths. Secondly, the quantum defect, defined as the part of the energy of the pumping photon, which is lost (not turned into photons at the lasing wavelength), is smaller than that of other common laser ions such as neodymium. When pumped at 975nm and emitting at 1060nm, the fraction of energy lost is 8.4%. This makes ytterbium laser more energy efficient than neodymium which has a 24% loss. Thirdly, Yb-doped silica fibers have a very broad emission band, from approximately 970nm to 1200nm, making them suitable for femtosecond pulse generation.

In this thesis, the Yb-doped fiber lasers are pumped with semiconductor laser arrays emitting at 975nm and emitting at around 1064nm.

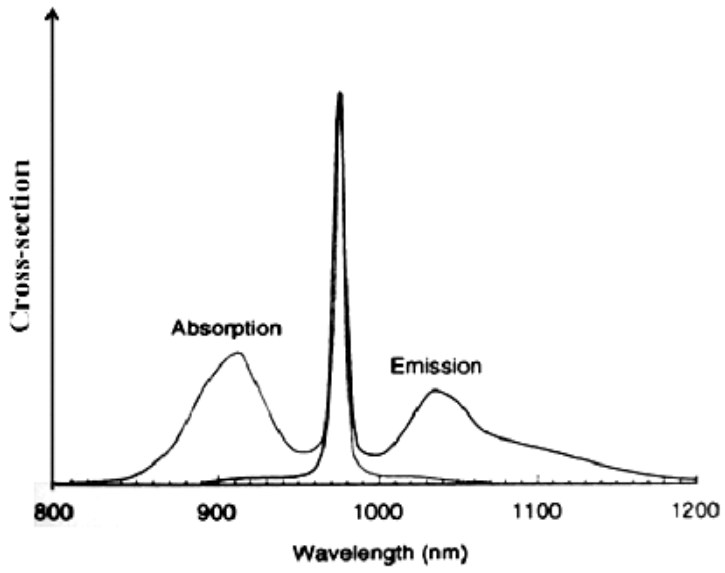

Figure 5. Yb absorption and emission band [18]

The fiber laser media used in our experiments are the double-clad type which consists of a single-mode core embedded in two layers of cladding layers, as shown in Fig. 6. The core is a single-mode waveguide doped with Yb^{3+} ions for generating laser radiation. The core diameter ranges from 5 microns to 20 microns and the numerical aperture is typically less than 0.1. The inner cladding is itself a waveguide of much larger numerical aperture and cross-sectional area for confining the pumping radiation. The pumping radiation traveling down the inner cladding is absorbed by the dopants in the core when the radiation repeatedly passes through the core.

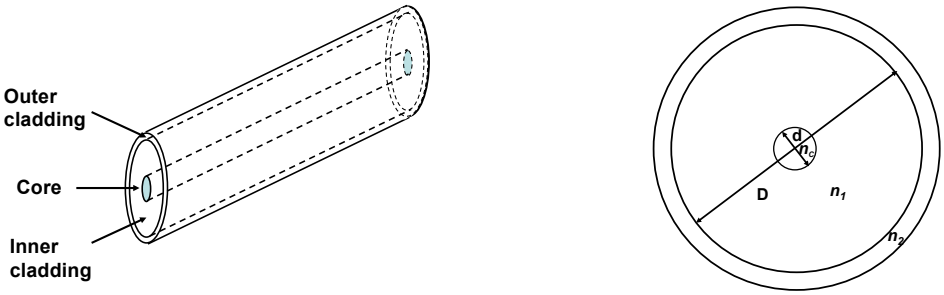

Figure 6. Double cladding fiber

This double-clad design has the advantage of being able to collect the pumping radiation more efficiently. Since the diode lasers used for pumping the fiber lasers are typically multimode laser arrays which behave like incoherent light sources and cannot be focused into the small single-mode core of the fiber. The use of large cross-sectional areas and large numerical aperture of the inner cladding improve the pumping efficiency by two orders of magnitude. The disadvantage is that, because the overlapping of the pumping radiation with the core is of the order of 0.1% to 10%, the fiber length needed to absorb all the pumping radiation is also longer,

which can result in higher losses associated with scattering and undesirable absorption in the core. For pulsed operation, the longer resonator length also results in longer pulse duration, making higher peak power harder to achieve.

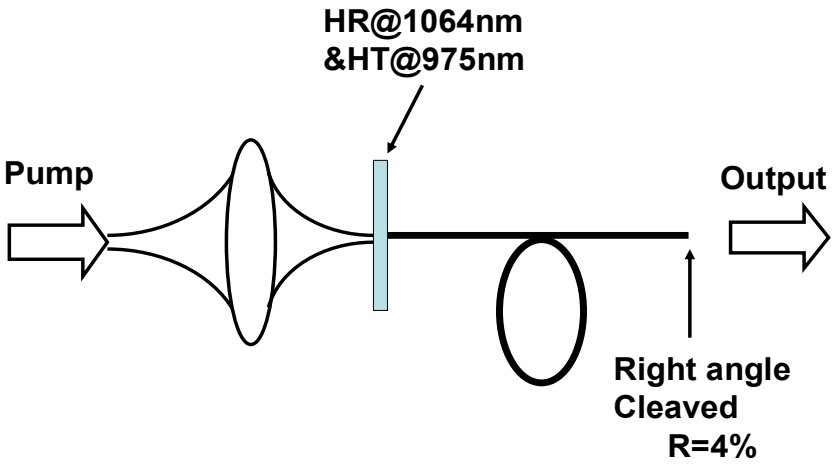

Figure 7. Schematic of a Yb-doped fiber laser

The schematic diagram of the end pumped Yb-doped fiber laser is shown in Fig. 7. The pumping end of the fiber is attached to a dielectric mirror with a high transmission at 975nm and high reflectance at 1064nm. The output end of the fiber is right-angle cleaved to give rise to a reflectance of 4% at the glass-air interface. Thus the resonator has a low Q-value.

2.2 Phase locking of two-element CW fiber laser array

From the phase control standpoint, the fiber laser arrays are different from laser arrays with fixed lengths, such as diode laser arrays and solid-state laser arrays, in their unequal and ever-changing path lengths among the fiber elements. The lengths of typical fiber lasers range from meters to tens of meters. It is practically impossible to ensure equal lengths in all the fibers in the arrays. The optical path lengths are also constantly changing due to uncontrollable thermal and mechanical effects. Assuming a thermal coefficient of path-length change of 10^{-5} / ^{o}C [19], a temperature drift of 0.01 ^{o}C can result in a phase shift of π in a 5-m-long silica fiber and totally alter the interference condition. Other uncontrollable disturbances to the fiber include mechanical vibrations, acoustic waves from someone speaking in the room, etc. An effective phase-locking technique must be able to response to the changes and maintain a stable beam profile.

Using a Fourier-transform resonator and a spatial filter, we have demonstrated that fiber lasers of arbitrary lengths can be stably phase locked to produce a diffraction-limited beam of the in-phase mode despite constant and random changes in the optical path length in the individual elements. The schematic of the experimental setup is shown in Fig. 8. [11] The fiber gain media are the Nufern PM-YDF-5/125 DOUBLE-CLAD Yb-doped fibers with a core diameter of 5 μm. The fiber lengths are 5.6 and 8.2 meters, respectively. The nominal numerical aperture is 0.46 for the inner cladding and 0.15 for the core. The small-signal absorption coefficient is 1.7dB/m at 975 nm. The fiber lasers are end pumped by two fiber-coupled laser diodes emitting at 972nm wavelength. The fibers are terminated at plane S_1 with a high reflectance mirror centered at 1064-nm wavelength. The other ends are perpendicularly cleaved. The reflectance of the cleave surface is 4%.

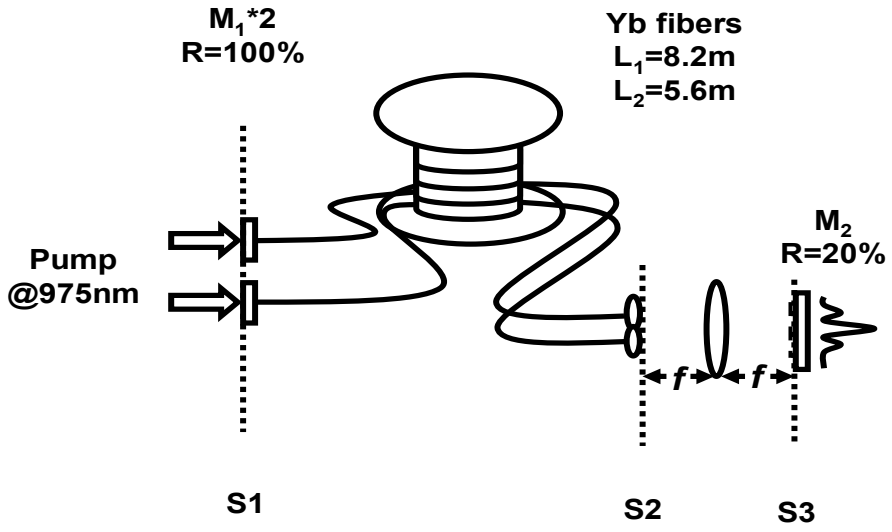

Figure 8. Experimental setup of phase locked two-element CW fiber laser array

The beams from the fiber ends are expanded to a diameter of 3 mm with a collimating lens. The collimated beams are positioned at the focal plane S_2 of a converging lens. The center-to-center separation between the two beams is 1.1 cm. The output mirror with a reflectance of 22% at 1064nm is placed at the other focal plane at S_3.

In the Fourier-transform resonator, the electric field profiles in the two focal planes at S_2 and S_3 are related to each other through a Fourier transformation. Since the Fourier transform of the near field (the light source) corresponds to that of the far field, the Fourier-transform resonator projects the far field of the light source (at S_2) to the output mirror. When the individual lasing elements operate in the same phase, constructive interference takes place at the center of the far field. When the elements are out of phase with a phase difference of π, the

center of the far field is dark. By placing a matching spatial filter, such as a thin wire, at the intensity peak of the out-of phase mode to cause higher losses, the laser can be forced to operate in the in-phase mode. For the convenience of being able to construct the spatial filter using easily available thin metal wires, the focal length is chosen to be 40 cm. A much shorter focal length may be used with finer grid patterns made by, for example, photolithography. The beam profiles in the near and far field are monitored using a charged-coupled device camera and a laser beam analyzer.

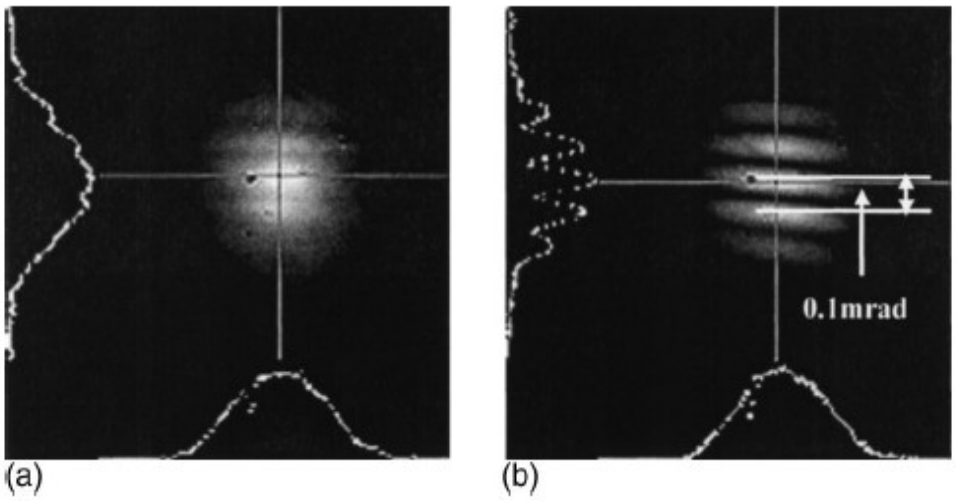

Figure. 9 Far-field images of : (a) free-running mode and (b) in-phase mode [11]

Fig. 9a shows the beam profile at the output mirror of the free-running laser array without a spatial filter. The beam profile exhibits low-contrast interference fringes that are constantly moving with irregular pace and direction. The pace of fringe movement exacerbates and the contrast further degrades when the individual fiber is subject to mechanical perturbations. To

stabilize the phase relation, a single gold wire is introduced as the spatial filter in front of the output mirror to create a higher loss for the out-of phase mode. Ideally, the best effect is achieved with a thinner wire at the first intensity minimum of the in-phase mode. For example, a 5-μm wire at the first intensity minimum of the in-phase mode would introduce an 8% loss to the out-of phase mode and 0.1% loss to the in-phase mode. For easier handling, a 12.75 μm wire is placed at the third intensity minimum of the in-phase mode to create 2.1% loss for the out-of phase mode and 0.2% loss for the in-phase mode. When the wire is moved across the beam at the output mirror, the position of the intensity minimum simply follows that of the gold wire. Fig. 9b shows the beam profiles of the in-phase mode. In the present experiment, a considerable fraction of the total energy is found outside the central intensity maximum. This is because the collimated laser beam width of the individual fiber lasers at plane S2 is 27% of that of the center-to-center distance between the beams, resulting in at least three lobes within the envelop of far-field intensity profile. More energy can be concentrated in the central lobe by increasing the width of the individual beams relative to the inter-element separation.

With the spatial filter in place, the phase locking is stable even when the optical path lengths are deliberately changed. For example, no slight fringe movement is observed when the temperature of one of the fibers is raised by 20 ^{o}C, which changes the relative optical path length by at least 200 wavelengths or when the fibers are shaken mechanically. It appears that a self-adjusting process has taken place to adapt to the changing environment.

2.3 Discussion and Conclusion

We have found that the phase-locked mode is highly stable despite the phase vibrations in the individual elements caused by thermal and mechanical effects. The ability to maintain phase locking is attributed to a self-adjusting process. The self-adjusting process can be understood in terms of selection of common resonances in a compound resonator. Fig. 10 illustrates the bandwidth of the longitudinal modes of two resonators of unequal lengths. The gain bandwidth of the Yb doped fiber is 5000 GHz which is extremely broad. The resonance frequencies of the waves in the fiber laser array, with individual lengths L_1 and L_2, must simultaneously satisfy the boundary conditions of having a node at plane S_1, due to the mirror's high reflectance, and having the same phase at plane S_2. Thus, the lasing frequencies are the common multiples of the free spectral ranges $c/(2nL_1)$ and $c/(2nL_2)$ of the individual fiber lasers.

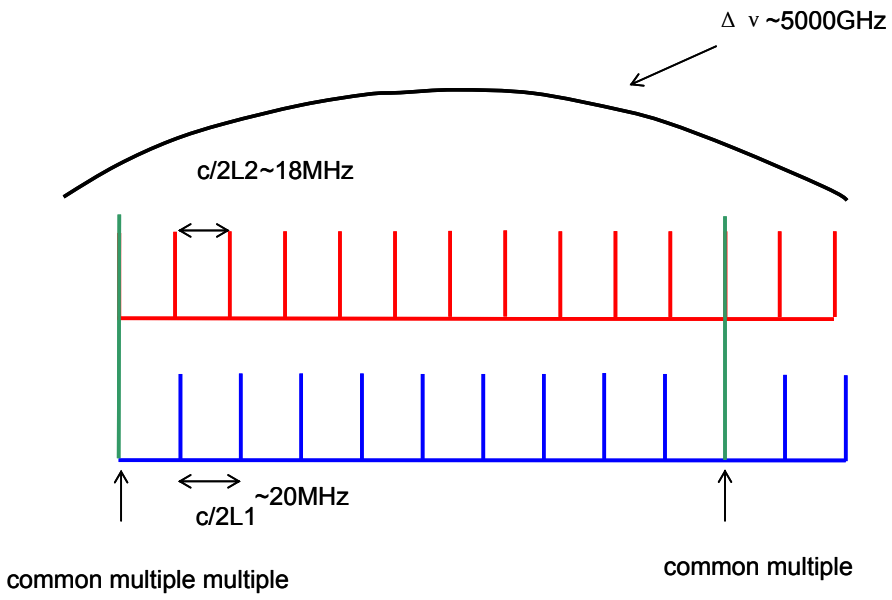

Figure 10. Longitudinal modes in two-element fiber laser array

When the optical path length of the elements changes, a new set of common resonances of the slightly shifted frequencies must emerge. This self-adjusting process is not always possible, but works best in laser systems with a combination of broad gain bandwidth, long and unequal lengths, and low-Q resonators. The broad bandwidth and long lengths provide a large number of closely spaced longitudinal modes within the gain bandwidth, making it easier to find the common resonances. The low-Q values of the resonator broaden the resonance lines to allow those with a small frequency mismatch to overlap. In the present case, there are 10^5 longitudinal modes within the gain bandwidth of the fiber laser with 5 m length. The fiber resonators with 100% and 4% reflectance at the end mirrors have a finesse value of 1.8. Thus all of the conditions favorable to the selection of common resonance frequencies are found in fiber lasers.

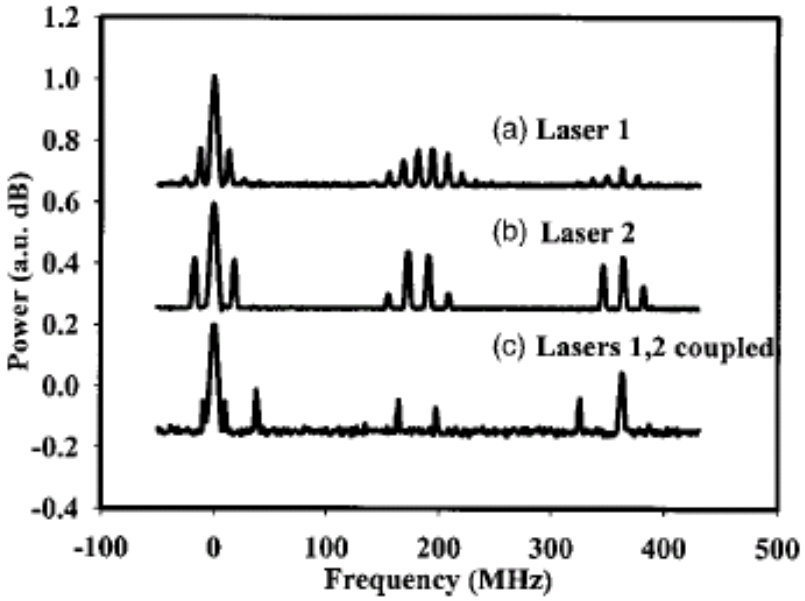

Figure 11. Spectra of intensity fluctuations of individual and phase-locked lasers [11]

To study the longitudinal mode spectra, the intensity fluctuations of the laser output are analyzed by using a radio-frequency spectrum analyzer. First, the output mirror is deliberately misaligned to decouple the two fiber lasers. The spectra of the beating waves of the individual lasers, shown in Fig. 11, consist of equal spaced peaks with an envelope modulation of 180MHz, which is caused by the 0.8-m-long external cavity. The peaks at 12.53 and 18.35 MHz, in (a) and (b) respectively, are the free spectral ranges of the fiber lasers of length L_1=8.2 m and L_2=5.6 m, respectively. When the output mirror is aligned to create the phase-locked mode, the spectrum of the beat waves exhibits fewer peaks at 38 MHz and its multiples at 153 and 198 MHz. In the present coupled system with a length difference of ΔL= 2.6 m, the minimum common multiple is predicted to be $\Delta v = c/(2n\Delta L)$ =39 MHz, which is consistent with the observed value of 38 MHz as shown in (c).

The outputs of the individual fiber lasers as well as the phase-locked laser array are unpolarized. In the present experiment, no special effort was made to align the polarization axes of the polarization maintaining fiber of the two fibers because a polarization eigen state can always be found in a two-element system regardless of relative orientation.

In conclusion, phase locking of two fiber lasers operating in the quasi-CW and CW mode with unequal and varying optical path lengths has been demonstrated. The stable phase locking is attributed to a self-adjusting process by which the laser array always operates in the common resonance frequencies of the composite resonator. The fact that the common frequencies can always be found in response to the changing environment is attributed to the fiber lasers having a unique combination of long cavity lengths, broad gain bandwidth and low Q resonators, which are favorable conditions for the formation of common resonance in the composite cavity.

Chapter 3

Phase locking in pulsed laser arrays

Chapter 2 is devoted to phase locking of the continuous-wave or long pulsed lasers with multiple gain elements and low-Q oscillators. For the continuous wave lasers, the phase-locked state is characterized by time-independent interference fringes in the far field where the laser beams from the individual elements overlap. To maintain a stable interference fringe pattern, all the elements in the phase-locked laser array must operate at the same frequency even though the optical path lengths of the individual elements may be different. As the coupling among the elements decreases or the frequency mismatching increases, the transition from the phase-locked state to the unlocked state is signified by an abrupt occurrence of multiple frequencies of the individual lasers due to the onset of oscillation of the individual lasing elements at slightly different frequencies [13].

In short-pulse lasers, however, the conditions for phase locking are expected to differ from those of the continuous-wave lasers in two ways. Firstly, two or more pulsed lasers operating in slightly different frequencies may still produce a stable interference fringe and considered to be phase locked as long as the fringe movement caused by the beat waves is smaller than the fringe spacing during the pulse. This effect may relax the requirement of equal frequency for all the elements. Secondly, the pulses generated by the individual elements having slightly different

lengths may not emerge simultaneously and may exhibit pulse distortion and the loss of spatial coherence in the combined output. This Chapter is devoted to phase locking of pulsed lasers. We have studied two different pulsed laser systems which represent two different regimes of the device parameters: a two-element fiber laser array generating nanosecond pulses through stimulated Brillouin scattering [14] and a two-element passively Q-switched laser array on a single crystal [15]. The former has a low-Q resonator with a short pulse duration (1 ns) compared to the round-trip time of pulses in the resonator (100 ns), while the latter has a high Q-value and a long pulse duration (5 ns) compared to the round-trip time (20 ps). Of great interest in the latter case are the tolerance of frequency differences between the lasers to maintain phase locking and the dynamics when the system is operated near the boundary of the phase-locked and unlocked states.

3.1 Short pulse generation in fiber lasers through stimulated Brillouin scattering (SBS)

SBS is an inelastic optical process in which the strong electric field of the laser wave interacts with the acoustic wave of the medium to generate the Stoke wave at a lower frequency and propagating predominantly in the opposite direction of the incoming laser wave. The frequency shift, Ω_B, satisfies the standard dispersion relation: $\Omega_B \approx 2\nu_A |K_p| \sin(\theta/2)$, where ν_A represents the acoustic velocity, K_p is wave vector of the pump laser and θ is the angle between the pump and Stokes fields. This equation shows that the frequency shift of the Stokes wave depends on the scattered angle. The shifted frequency Ω_B is maximum in the backward direction ($\theta = \pi$) and vanishes in the forward direction ($\theta = 0$). In a single-mode fiber, there are only two relevant directions, either forward or backward. For this reason, SBS occurs

predominantly in the backward direction. The Stokes wave has a frequency shift of about 10 GHz in silica glass which is smaller than the width of the laser gain media. Thus the SBS pulses generated in fiber lasers can be amplified by the fiber gain media.

The generation of the Stoke wave can be understood as the incoming laser wave being reflected (or diffracted in the backward direction) from the traveling Bragg grating, which is a periodic refractive index modulation caused by the acoustic wave through electrostriction in silica glass. The acoustic wave is in turn generated by the beat wave resulting from the beating of the laser wave and the Stokes wave. In silica fibers, the threshold of SBS is about 1W for a 10-m-long fiber with a 5-μm-diameter core. The threshold is expected to be much lower in fiber lasers because the gain medium that amplifies the laser radiation also amplifies the Stoke wave.

There have been a number of reports of a Q-switching-like mechanism based on SBS for generating extremely intense short pulses in fiber lasers. This mechanism works as follows: The reflectivity of the traveling Bragg grating depends on the depth of the refractive-index modulation. As the intensity of the Stoke wave increases, so does the refractive-index modulation as well as the reflectivity of the Bragg grating, which results in further amplification of the Stoke wave. This is a runaway process that eventually leads to total conversion of the energy from the laser wave into Stoke wave by the traveling Bragg grating.

Unlike conventional Q-switching fiber lasers in which the pulse duration is proportional to the length of the resonator, the duration of the pulses generated by SBS does not depend on the length of the resonator but rather on the dynamics of the nonlinear process. For example, short pulses of 2 – 5 ns duration have been demonstrated in fiber lasers whose round-trip time is of the order of 100 ns [1-4].

Short pulse generation through stimulated Brillouin scattering in fiber lasers is a self-starting process that does not require an intracavity modulator, but the occurrence of pulses is highly irregular in pulse energy, shape and repetition rates [3,4]. The pulse dynamics may be stabilized by using an active or passive intracavity modulator to induce Q-switched laser pulses [2,3] which in turn, initiate the SBS process. When the SBS pulses are initiated by the intense Q-switched laser pulse, their repetition rates also follow those of the Q-switched pulses.

In our experiment [14], a 1-mm-thick Cr^{4+}: YAG (yttrium aluminum garnet) crystal is used as a saturable absorber to induce Q-switching. The Cr^{4+}: YAG crystal provides a large absorption cross section in the 0.9-1.2 μm spectral region. The absorption coefficient in Cr^{4+}: YAG decreases with increasing light intensity when the power density reaches MW/cm^2.

The schematic of the Q-switched fiber laser for short pulse generation through stimulated Brillouin scattering is shown in Fig. 12.

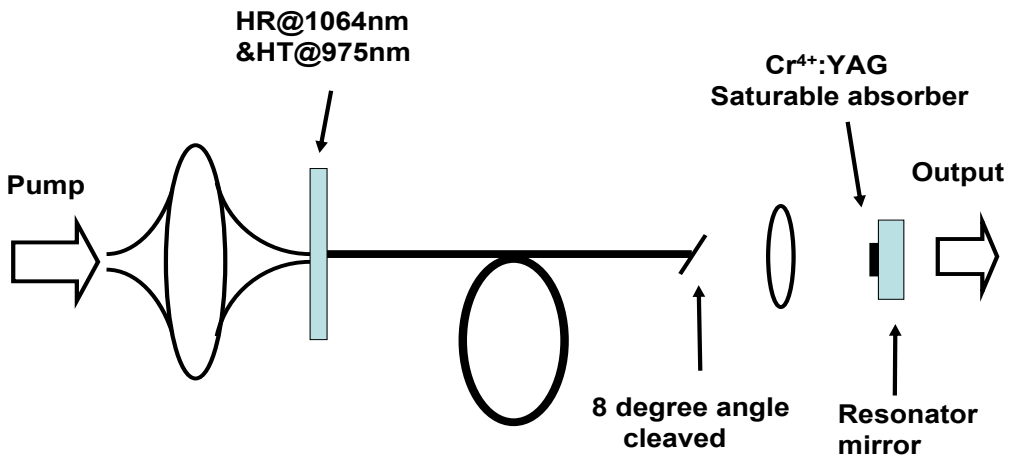

Figure 12. Experimental setup for stabilized SBS pulse generation

The fiber laser is similar to that described in Chapter 2 except that the output end of the fiber is angle-cleaved at 8 degrees to suppress the optical feedback from the fiber ends. By eliminating the feedback from the end of the fiber, the fiber can absorb higher pump energy without lasing and the fiber gain medium can achieve higher gain to help reduce the threshold for the onset of SBS process. The saturable absorber with an unsaturated transmission of 50% is placed in front of the output mirror. When the pump power reaches the threshold of 0.5W, a stable train of Q-switched pulses is observed. The pulse duration is 1μs and the pulse energy stays nearly constant as the pump power increases. The characteristic of the pulses are quite typical of those found in passively Q-switched lasers. Due to the long pulse duration, the peak power of Q-switched fiber laser is low and not very useful.

The onset of SBS process needs even higher gain in the fiber. The gain can be raised by misaligning the resonator mirror while keeping a higher pump power. When the gain reaches a sufficiently high level for the onset of SBS process, the train of long Q-switched pulses evolves into a train of intense pulses of 1.5-ns pulse duration. The intense SBS pulses have ten times the pulse energy of the long Q-switched pulses and ultimately truncate the long pulses that initiate them. Since the SBS pulses are initiated by the Q-switched pulses, they exhibit more regular pulse-to-pulse separation. Each SBS pulse has about 5 μJ pulse energy with a corresponding power density of 17 GW/cm^2 in the fiber core which is close to the 20 GW/cm^2 optical damage threshold on the air-glass interface of the fiber ends. And indeed the fiber ends are often damaged by the laser pulses during our experiment.

3.2 Phase locking of SBS pulses in two-element fiber laser array

This section is devoted to a study of phase-locked operation of stimulated Brillouin backscattering in two Yb-doped double-clad fiber lasers. This system differs from the continuous-wave lasers described in Chapter 2 in three ways: (1) The development of SBS pulses is known to be stochastic. It is a challenge to ensure the SBS pulses emerging from the individual elements simultaneously. (2) The Stokes pulses are frequency-shifted from the primary pulses by about 10 GHz, which is far larger than the frequency spacing of the longitudinal modes and have different resonance conditions. Phase locking of frequency-shifted pulses have never been attempted before. (3) The SBS pulses are much shorter than the round-trip time of the fiber resonator. The mismatch in the lengths of the two fibers is expected to affect the dynamics of phase locking.

The schematic of the experiment setup is shown in Fig. 13.

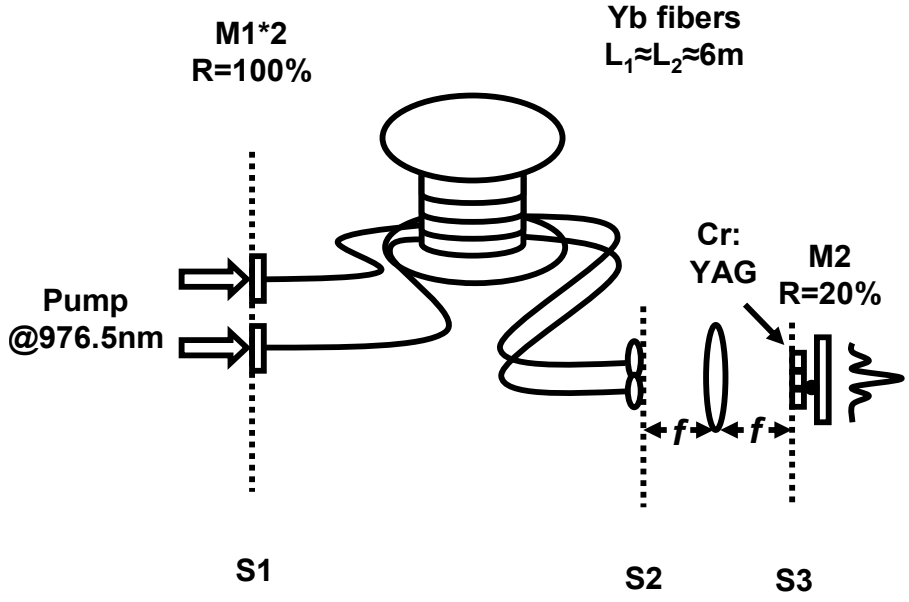

Figure 13. Experimental setup for phase-locking of SBS pulses in two-element fiber laser array [14]

The fiber gain media are two Nufern PM-YDF-5/125 double-clad Yb-doped fibers with a core diameter of 5 μm. The numerical aperture is 0.46 for the inner cladding and 0.15 for the core. The two fibers are approximately 6 m long. The small-signal absorption is 1.7dB/m at the pump wavelength of 975 nm. The resonator mirrors at the pump end have high transmission at 976 nm and nearly 100% reflectance at 1064 nm. The other ends are angle cleaved at 8 degrees to suppress the optical feedback from the fiber ends. The beams from the fibers are expanded to 3-mm diameter and coupled to a Fourier-transform resonator. A 1-mm-thick Cr: YAG saturable absorber with an unsaturated transmission of 50% at 1064 nm is placed in front of the output mirror to induce Q-switching. The pump diode lasers are operated in the quasi-continuous- wave mode with 700 μs duration and 60 Hz repetition rate. When the pump power in each fiber laser reaches 0.5W, a train of Q-switched pulses is observed. The pulse duration is 1μs and the pulse energy stays nearly constant as the pump power increases.

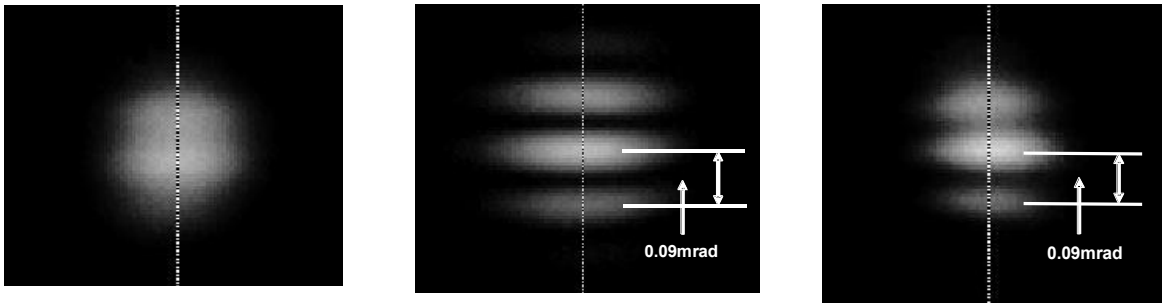

(a) (b) (c)

Figure 14. Beam profiles at the output mirror of (a) free-running SBS pulses (b) phase-locked Q-switched laser pulses, (c) phase-locked SBS pulses [14].

With the aid of a charge-coupled device (CCD) camera and a laser beam analyzer, we examined the beam profile of the output at focal plane S3. The results are shown in Fig. 14(a). The beam profile exhibits low-contrast interference fringes that are constantly moving from pulse to pulse.

To stabilize the phase relation, we introduce a 5-μm gold wire in front of the output mirror along one of the dark fringes of the in-phase mode as the spatial filter to create a higher loss for the out-of-phase mode. Fig. 14(b) shows the beam profile of the phase locked laser array with Q-switched laser pulses when stabilized by a spatial filter. The contrast of the interference fringes is nearly 1 and remains unchanged with time. The fringe spacing is 18 μm.

When the output mirror is slightly misaligned from its optimal position while keeping a higher level of pump energy, the gain in the fibers increases and SBS pulses are observed. The pulses have a 1.5-ns pulse duration and much higher peak power with about ten times of the pulse energy as primary Q-switched pulses. With arbitrarily chosen fiber lengths, the giant pulses from the two fiber lasers cannot be phase locked and the beam profile at the output mirror exhibits poor contrast ratio, as shown in Fig. 14(a). The oscilloscope traces of the outputs of individual lasers are shown in Fig. 15(a). The pulses from the individual fibers appear to be occur independent from each other and therefore do not overlap in time.

The interference fringes can be stabilized when the difference in lengths of the two fiber resonators is less than 2 cm. Fig. 14(c) shows the beam profile at the output mirror when the two fiber lasers are operated in phase. The oscilloscope traces also confirm the coincidence of the pulses from the individual lasers as shown in Fig. 15(b).

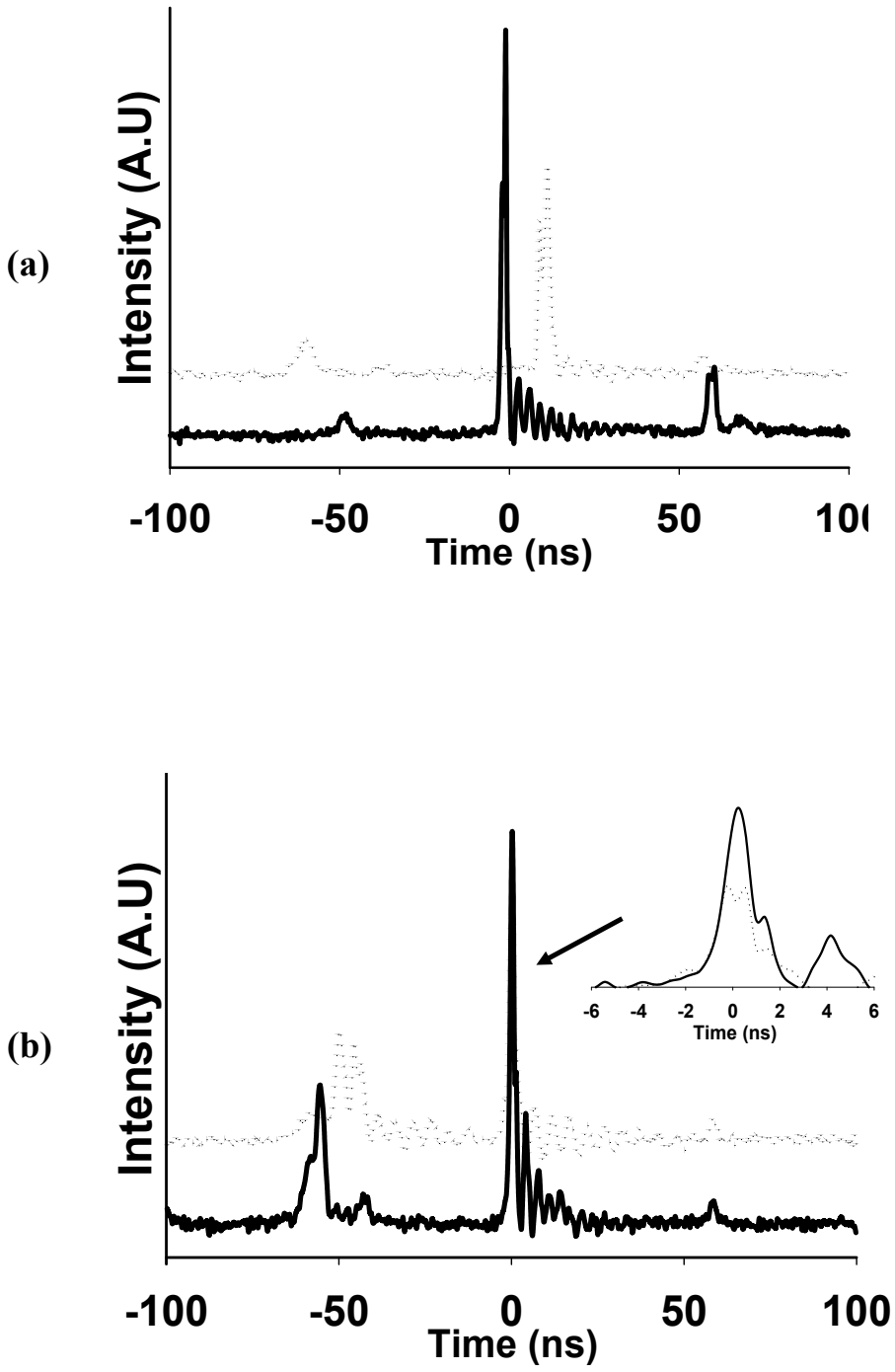

Figure 15. Oscilloscope traces of the laser pulses from two fiber lasers when they are phase (a) unlocked and (b) locked [14]

The time series of the output pulses also shows that the pulse duration in the final stage of development leading to the strongest pulse is much shorter than the round-trip time in the fiber cavity. The round trip amplification is about 10. Thus a two-element laser system is essentially a two-armed laser amplifier for free-propagating pulses during the final stage. Any unevenness in the waveguide and pump level can result in unbalanced output pulse energy from each fiber, as illustrated by the inset in Fig. 15, and the destructive interference being not totally dark. This explains the lower contrast ratio of the beam profile at the output mirror, compared to those for the conventional Q-switched laser pulses.

3.3 Discussion and Conclusion

From the experimental observations, we have reached the following understanding of how the SBS pulses are phase locked. The relevant parameters are sketched in Fig. 16.

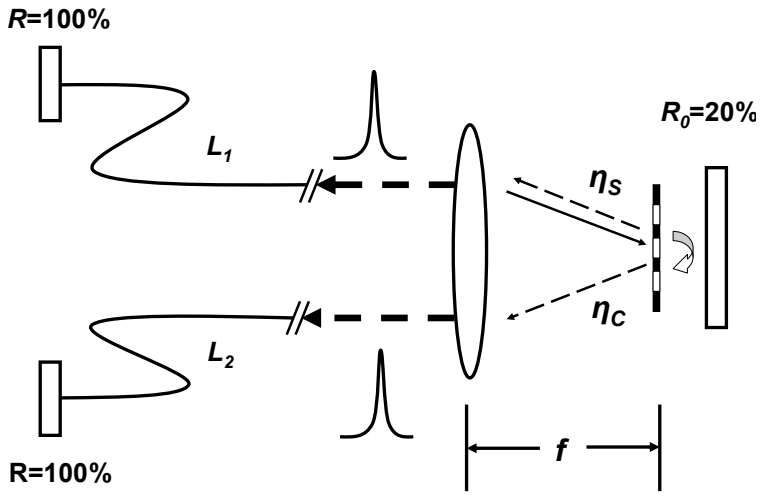

Figure 16. Two-element fiber lasers coupled through a diffractive element in an external resonator [14]

(1) At the very beginning, passively Q-switched pulses are generated in the fiber lasers due to the action of the saturable absorption in Cr: YAG. The pulses would have a microsecond duration, if the pulses were allowed to run their course without being truncated by the SBS. Due to the long pulse duration of one microsecond compared to the round-trip time of 100 nanoseconds in the optical fiber, the Q-switched pulses from the two fiber lasers overlap in time and establish an interference fringe when they meet at the output mirror. The presence of the spatial filter forces the two lasers to operate in the same phase.

(2) When the leading edges of the Q-switched pulses bleach the saturable absorber, the interference fringe is "written" to the saturable absorber and creates a periodic pattern of bleached regions which behave as a loss grating where the bleached regions have lower absorption loss and unbleached regions have higher loss. The loss grating serves two roles: diffractive optical feedback for the individual fiber lasers and cross coupling between the lasers. The diffractive feedback has a self-coupling efficiency η_S and cross coupling has a cross coupling efficiency $\eta_C = 1 - \eta_S$, as illustrated in Fig. 16.

(3) When the intensity of the Q-switched lasers pulses is high enough to initiate the SBS process, a frequency-shifted Stokes pulse is generated. In a two-element fiber laser array with lengths L_1 and L_2 coupled to an external resonator, there are three resonators, with gain lengths L_1, L_2 and L_1+L_2, sharing the common gain media. In the absence of the self-coupling, η_s , the resonator with length L_1+L_2 would have the largest gain length and the lowest threshold for the SBS process. The SBS pulses thus created would be propagating in the two fibers sequentially and the output from the fibers can not be phase locked. In the present experiment, the first order diffraction of the loss grating in the saturable absorber provides a self-coupling strength of approximately 30% and cross coupling strength of 70% assuming a full saturation of the

saturable loss. This enables the SBS pulses initiated in one of the arms of the gain media to become the seeds for amplification in both arms of the gain medium simultaneously and their interaction through the diffractive element in the common external resonator can result in phase locking. Since the pulse duration of the SBS pulses is much shorter than the round-trip time in the individual resonator, effective phase locking also requires that the difference in fiber lengths be much less than the pulse duration.

In the present study, the combined peak power is 6.67 kW, corresponding to a power density of 17 GW/cm^2 in each fiber which is already near the threshold of optical damage. Further increase in pulse energy in each fiber laser, which is achievable by further misaligning the output mirror while keeping higher pump energy, would result in a definite optical damage in the fiber ends. The pulse energy of the phase locked mode for the coherently combined pulses is 10 μJ which is two times the pulse energy of the individual fiber lasers. The efficiency of coherent beam combination is high. This points to the possibility of a coherent combination of intense lasers pulses generated by nonlinear processes in multiple fiber lasers to achieve higher brightness much beyond the power density of optical damage of a single fiber.

3.4 Phase locking of Q-switched pulses in microchip lasers

The previous sections in this chapter are devoted to phase locking of two SBS pulses whose durations are much shorter than the round-trip time of the laser pulses traveling in the laser cavity. In fiber laser arrays with several meters of fiber lengths, there are a large number of longitudinal modes, on the order of 10^5 within the gain bandwidth of the Yb-doped fibers. Thus it is always possible to find longitudinal modes whose frequencies satisfy the resonance conditions

in all elements in the array. Our study finds that the only condition that must be met for phase locking to take place is that the two fibers have nearly the same length so that the pulses emerge simultaneously.

An unanswered question is how and whether the pulsed lasers can be phase locked if the common resonance frequencies cannot be found. This situation can occur in microchip lasers whose cavity lengths are on the order of millimeters and there are few longitudinal modes within the bandwidth of the gain media. This Section is devoted to a study of phase locking in a two-element Q-switched microchip laser array.

In short-pulse lasers, two or more pulsed lasers operating at slightly different frequencies may still produce a stable interference fringe. Using a two-element pulsed laser array as an example, the maximum frequency mismatch to allow a temporally stable fringe pattern is determined by the rate at which the beat waves sweep through half the fringe spacing or $1/(2\tau)$, where τ is the duration of the pulses. Based on this argument, the upper limit of frequency mismatch among the elements in a Q-switched laser array generating 5-nanosecond pulses is on the order of 10 MHz. But the pulses generated by the individual elements operating at slightly different frequencies may not emerge simultaneously, which can result in a loss of spatial coherence. Thus near the boundary of phase locking, we expect a regime of partial spatial coherence.

Q-switched microchip laser

We have conducted a study on phase locking in a two-element Q-switched microchip laser array. The monolithic passively Q-switched Cr, Nd:YAG laser was first developed in our laboratory [20]. When pumped by diode lasers emitting at 808-nm wavelength, the laser generates nanosecond pulses in a single longitudinal mode. The monolithic resonator has no

moving parts and thus the output is extremely stable. The pulse-to-pulse power fluctuation is less than 0.3% which is hardly detectable with a digital oscilloscope. The monolithic system permits us to control the frequency difference very precisely and continuously and observe the dynamics of laser pulses near the boundary of phase-locked and unlocked regions.

The schematic of the Q-switched microchip laser is shown in Fig. 17. The laser crystal is a 2-mm-thick Cr,Nd:YAG in which the Cr^{4+} ions act as the saturable absorbers for the neodymium laser emission at 1064nm. The neodymium concentration is 1.1-wt%. The chromium concentration is unknown but the unsaturated absorption coefficient caused by chromium is 0.21 cm^{-1} at 1064 nm. The laser crystal is polished to form a flat–flat Fabry–Perot cavity. The pump facet is coated for high transmission at 808nm and high reflection at 1064 nm. The output facet is coated for 97% reflectivity at 1064 nm and high reflection at 808 nm to allow double passes of the pump beams within the gain medium. Due to a small deviation from perfect parallelism between the two end surfaces of the laser crystal, the laser cavity length is slightly variable by pumping different locations on the crystal. The frequency of the single laser can be continuously detuned over several GHz by rotating the crystal around the axis.

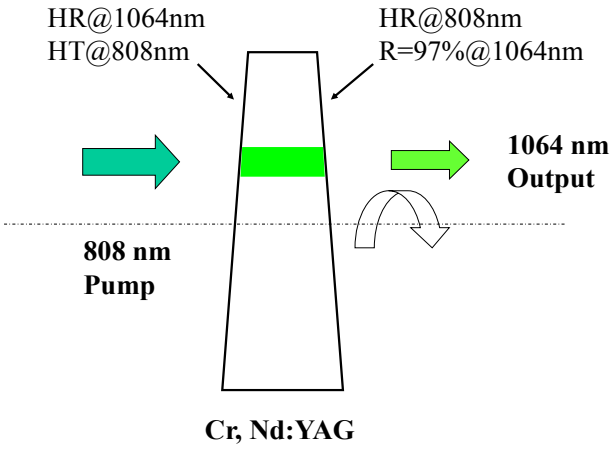

Figure 17. Schematic of the continuously tunable Q-switched laser

Q-switched microchip laser array

The schematic of the two-element Q-switched laser array is shown in Fig. 18. The lasers are end-pumped by diode laser beams through two optical fibers, each delivering 1.5W at 808 nm. The pumping diodes are operated in the quasi-CW mode with 300μs pulse duration and at a repetition rate of 100 Hz. The diameter of the pumped region is approximately 200 μm. The maximum output pulse energy is 10 μJ per element.

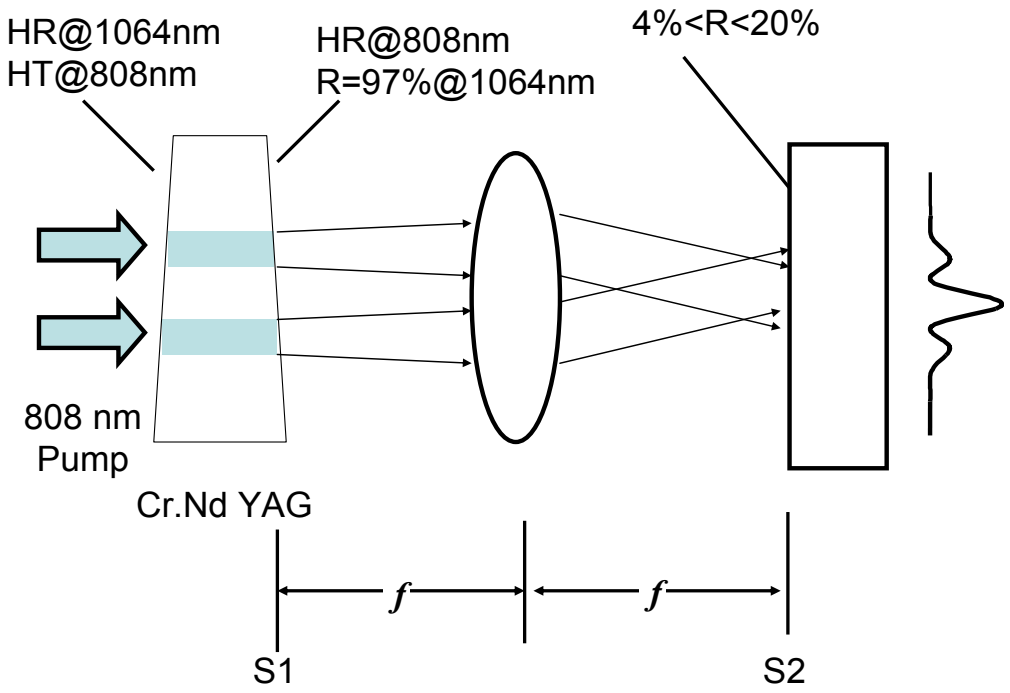

Figure 18. Schematic of the coupled Q-switched lasers [15]

The center-to-center separation between these two fibers is chosen to be 500 μm. At this separation, the far-field pattern when the two lasers are operating simultaneously is identical to those of the individual elements, as shown in Fig. 19(a), indicating that the coupling between the

lasers through evanescent waves is negligible. The lasers are coupled to a Fourier-transform resonator which allows the relative phase of the laser elements to be stabilized by controlling the far-field pattern at the output mirror. The output facet of the laser crystal is placed at one focal plane S1 of the converging lens and the output mirror is placed at the other focal plane S2. The focal length of the lens is 10 cm. A 1-cm thick etalon (not shown) with a finesse of 60 at the lasing wavelength is used to analyze the lasing spectra. The beam profiles at the output mirror at S2 and the interference fringes after the etalon are monitored by two charge-coupled-device cameras. Three fast photodiodes are used to detect the output of the individual elements and the combined output.

In the absence of optical feedback from the resonator, the lasers generate Q-switched pulses in the TEM_{00} mode and a single longitudinal mode with pulse duration of 5.5 ns. The combined pulse energy from the two elements at the output is 20 μJ. The time series of the output exhibits two sets of pulse trains. The timing jitter of the pulses relative to the front edge of the pump pulse is on the order of 1 μs. Fig. 19(a) shows the beam profile at the output mirror of the free-running lasers which is the incoherent addition of the far field profiles of the individual lasers. The frequency difference between the two lasers can be adjusted continuously from zero to 1 GHz by rotating the crystal around the axis by 90 degrees. The resolution of the etalon is 160 MHz. Smaller frequency differences that cannot be resolved by the etalon can be inferred from the angular position of the laser crystal measured from the position of zero detuning. From the maximum frequency difference of two lasers separated by 500 microns, we estimate the maximum wedge angle between the end surfaces to be 7 arc seconds.

(a)

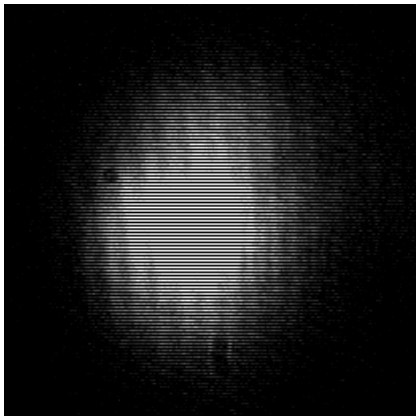

(b)

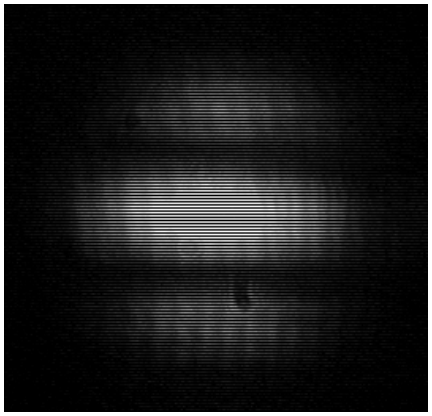

(c)

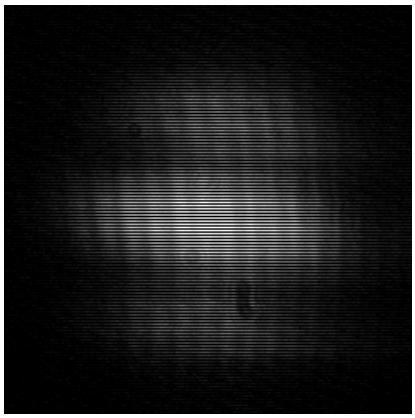

Figure 19. Beam patterns of the two lasers operating (a) in the free-running state without the external resonator, (b) in the phase-locked state with zero frequency mismatch and (c) in the phase-locked state with a frequency mismatch of 20 MHz. [15]

When the external cavity is properly aligned and the frequency mismatch set to zero, the two lasers generate pulses with equal intensity and perfect coincidence. The beam profile of the two lasers at the output mirror S2 exhibits the fringe pattern of either the in-phase or out-of-phase modes. The patterns irregularly switch between the two modes from shot to shot. The fringe spacing is 160 μm, which is consistent with that calculated from the 500 μm separation of the two laser emitters and the 10 cm focal length of the external resonator. To stabilize the phase relation, a single 65-μm-diameter wire is placed in front of the output mirror as the spatial filter to create a higher loss for the out-of-phase mode. With the filter in place, the contrast ratio of the fringe pattern increases dramatically and the pattern remains stationary. Fig. 19 (b) shows the beam profile of the in-phase mode. The total output pulse energy of the phase locked laser is 26 μJ, which is 30% higher than the total pulse energy of the free-running. Fig. 20(a) shows the oscilloscope traces of the pulses from individual elements when the detuning is nearly zero. Under this condition, the two pulses coincide precisely in time.

As the frequency mismatch between the two elements increases, the fringe contrast at the output mirror gradually deteriorates. The combined output also successively exhibits pulse broadening, double pulsing, and complete separation of pulses as the detuning increases. As an example, the far-field pattern of reduced contrast taken at $\Delta\nu$=20 MHz is shown in Fig. 19(c). The corresponding oscilloscope traces of the pulses from individual elements are shown in Fig. 20(b). The reduced fringe contrast and broadened pulses are due to the emergence of a relative time delay between the pulses from the individual elements.

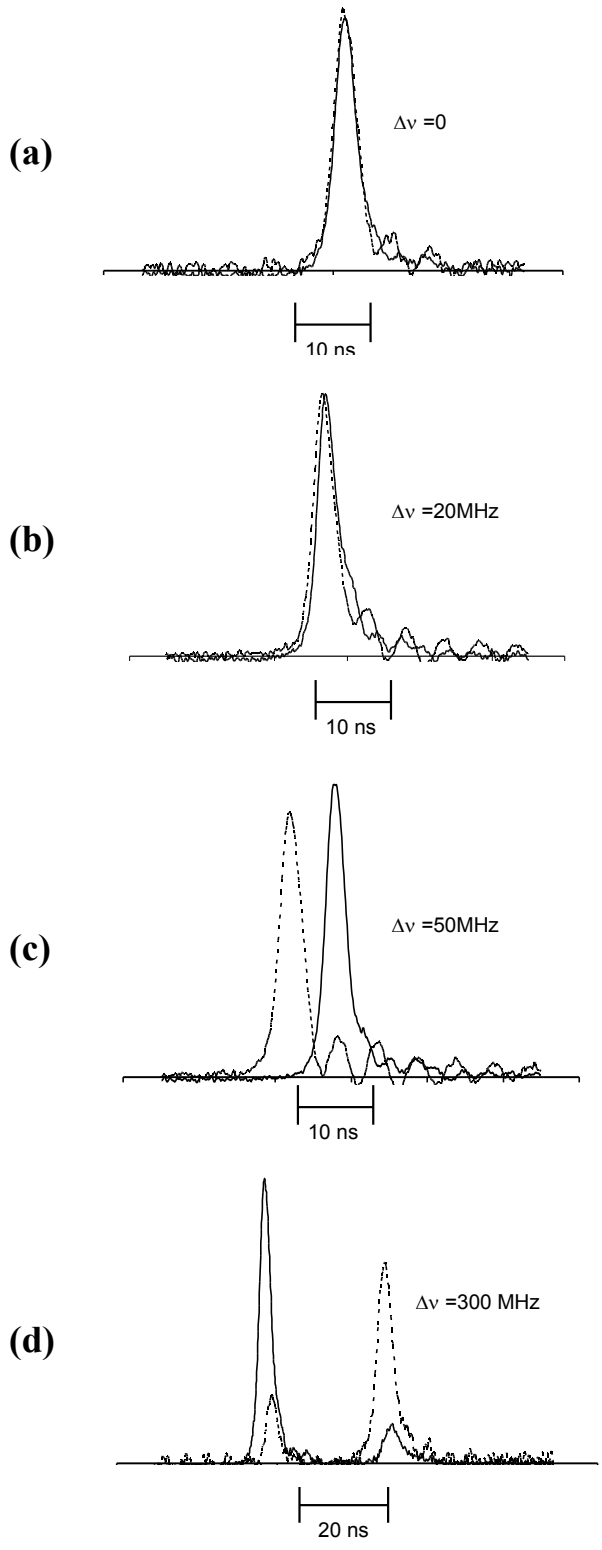

Figure 20. Oscilloscope traces of phase-locked Q-switched pulses with (a) zero frequency mismatch and frequency mismatches of (b) 20 MHz, (c) 50 MHz and (d) 300 MHz. [15]

The relative time delay increases with increasing frequency mismatch and the two pulses become completely separated in time at $\Delta\nu$=50 HMz, as shown in Fig. 20(c). With increasing frequency mismatch and decreasing optical feedback, by misaligning the external cavity mirror, a relative delay as large as 50 ns has been observed. An example of the pulse pairs separated by 20 ns at $\Delta\nu$= 300 MHz is shown in Fig. 20(d). The relative timing jitter between the pulse pair is zero. The trailing pulse appears to be initiated by the leading pulse, and here we have a situation of two pulses being temporally coherent and spatially incoherent.

3.5 Discussion and Conclusion

The observed dynamics of the phase-locked mode and transition between the locked and unlocked states can be explained based on the competition among the various modes in the laser array. Although the passively Q-switched laser pulses are only 5 nanoseconds in duration, the process of laser intensity amplification from the initial spontaneous emission to the intensity level which is strong enough to bleach the saturable absorber is long. Thus the mode selection during the building-up period follows the same mechanism as in the CW lasers.

We base our discussion on the model of two lasers of unequal lengths coupled to an external resonator as illustrated in Fig. 21. When the two elements have unequal lengths, the operating frequencies cannot satisfy the resonance conditions in both elements simultaneously and the model profiles of the transverse modes are determined by the proximity of the frequencies to the nearest longitudinal modes. The symmetric modes, presumably resonating with the cavity whose length is the average of the two, generate two pulses of equal amplitudes in the individual

elements simultaneously. However, the symmetric modes, being off resonance in both elements, are not favored unless the two elements are nearly equal in lengths.

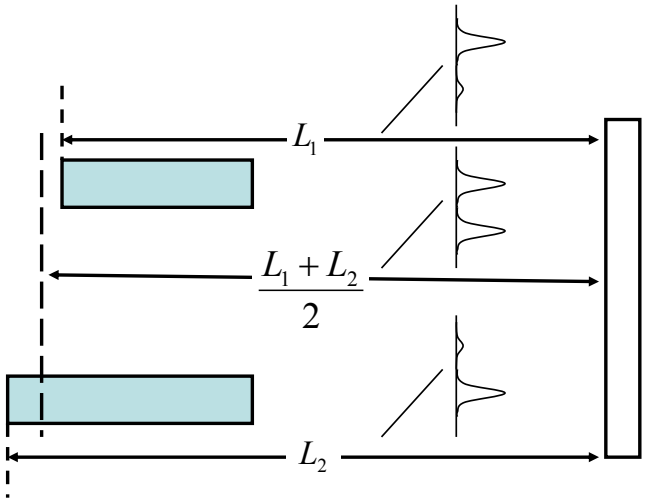

Figure 21. Diagrams illustrating two lasers of unequal lengths coupled to a common external resonator and the intensity profiles of various spatial modes. [15]

In the presence of a large frequency mismatch, the dominating modes are expected to operate at the frequencies in the vicinity of the resonances of the individual elements. The spatial profiles of these modes are asymmetric with the stronger intensity residing in the element which is closer to resonance. The saturation of the saturable absorber further enhances the stronger element due to the reduced absorption loss caused by the stronger intensity. This process leads to the Q-switching pulse appearing in one of the elements first. The leading pulse then initiates the pulse in the other element, at a slightly different center frequency, by the coupling through the external resonator. The coupling is an injection seeding process whose strength depends on the frequency mismatch relative to the spectral bandwidth of the laser pulse. When the resonance

frequency of one of the elements falls within the spectral bandwidth of the laser, which is estimated to be 60 MHz, the coupling is strong and the relative time delay of the pulses can be smaller than the pulse duration. These partially overlapping pulses create a stable interference fringe but with reduced contrast ratio. When the frequency mismatch is larger than the spectral bandwidth, the coupling is weak and the trailing pulse can be totally separated from the leading pulse. Because the trailing pulse is injection seeded by the leading pulse, the relative timing jitter between these two pulses is nearly zero even though the pulses are widely separated in time.

The study shows that the frequency mismatch in the Q-switched laser array causes a relative time delay between the pulses from the individual elements. The trailing pulses are initiated by the leading pulse and, for a given frequency mismatch, maintains a fixed time delay without a timing jitter. This results in a situation where the pulses from the individual element are temporally coherent but spatially incoherent. To create phase locking with a high degree of spatial coherence, which is needed for most applications, the frequency mismatch must be reduced to much less than spectral bandwidth of the laser pulses. To achieve a frequency mismatch of less than 20 MHz between two elements separated by 500 μm, the two planar surfaces of the laser crystal must be parallel to within 0.14 arc second, which cannot be guaranteed using standard polishing technique. This stringent requirement of parallelism rules out the possibility of forming a two-dimensional phase-locked solid-state laser array in a single crystal, but still permits one-dimensional laser array to be formed along the direction of minimum wedge angle.

Chapter 4

An application of miniature Q-switched laser: High-resolution photoacoustic imaging

This Chapter is devoted to an application of the short-pulse solid-state lasers developed in our laboratory to biomedical imaging. An area which we have achieved considerable success is the demonstration of high-resolution photoacoustic imaging, which combines light and ultrasound to generate images. The combination has led to higher image resolution than that achievable with traditional pulse-echo ultrasound and new capabilities that are not available with light or ultrasound sound alone. The initial intended application is for diagnostic imaging of the eye. The system is also useful for imaging of superficial tissues such as the skin and any tissues that are accessible through an endoscope.

4.1 Traditional ultrasound imaging technique

Ultrasound imaging is commonly performed in pulse-echo mode, as illustrated in Fig. 22, in which a short acoustic pulse is emitted by a transducer and reflections or echoes are generated whenever the ultrasound encounters a change in acoustic impedance (density x speed-of-sound). The echoes are then detected by the same transducer. The transit time of the

echo signal is proportional to the distance between the target and transducer. The time series of the echo signals generated by a single ultrasound contains a one dimensional image in the axial direction. B-scan generates a two-dimensional cross-sectional image by moving the transducer laterally in small increments while acquiring the one-dimensional (axial) images at each stop along the way. An example of the B-scan image of an ex-vivo pig eye is shown in Fig. 23. In Fig. 23(a), the ultrasound pulses travel from top to bottom, as indicated by the dashed arrow. The bright layers are the front surface of cornea, back surface of the cornea, and front surface of the lens, respectively. In Fig. 23(b) the time series of the detected reflection signal is superimposed on the image.

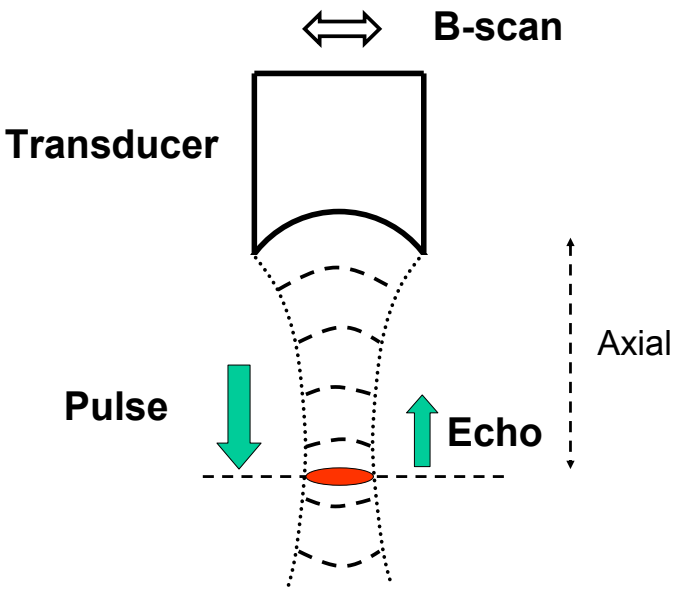

Figure 22. Pulse-echo ultrasound imaging

Ultrasound biomicroscopy refers to imaging at frequencies of 30 MHz or higher that have been used for high-resolution imaging of the eye and skin [21-23]. Like all detection techniques based on waves, the lateral resolution is determined by $1.22 \times F\frac{\lambda}{D}$,where $\boldsymbol{\lambda}$ represents the wavelength, *F* and *D* represent the focal length and diameter of the focusing transducer.

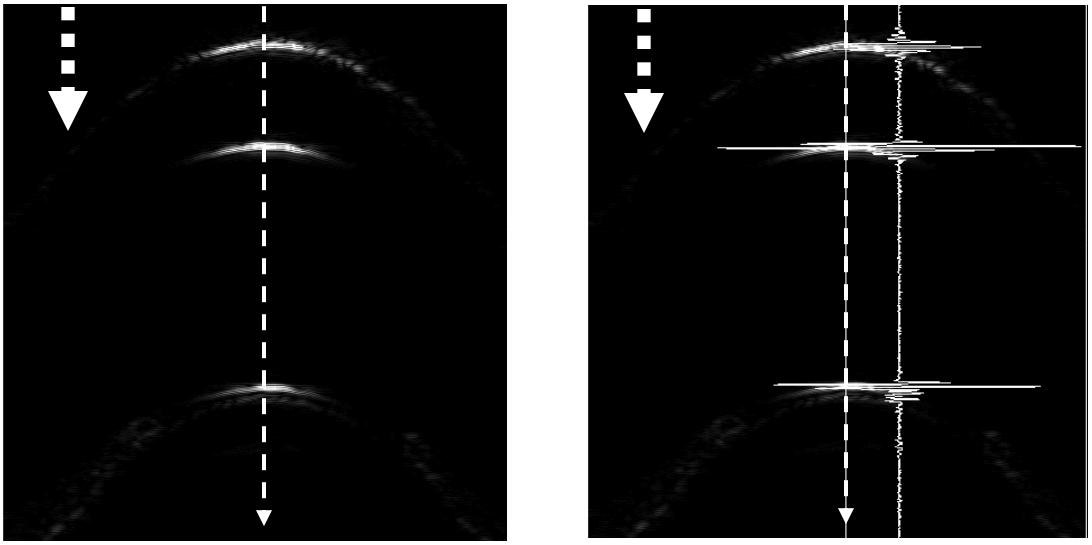

(a) **(b)**

Figure 23. B-scan of an ex-vivo pig eye at cornea and front surface of lens

For transducers having a center frequency of 20 MHz or (wavelength = 70 microns), the resolution is on the order of 200 microns. Although the resolution may be improved by using a higher frequency transducer, the rapid increase of attenuation coefficient with frequency in water ($\alpha = 2 \times l \times 0.0022 \times f^2\ dB$ where l is the range measured in centimeters and frequency f in MHz) sets the limit for useful operating frequency to about 50 MHz [24]. Thus ultrasound alone

cannot resolve fine and essential features, such as microvasculatures in optical nerves in retina which are typically 50 to 250 μm in diameter.

4.2 High-resolution photoacoustic imaging technique

In photoacoustic imaging [25-29], a short laser pulse is directed at a tissue and the absorption of the laser pulse by chromophore causing the temperature in the tissue to increase. The thermal expansion generates a pressure wave which propagates outward in the form of broadband ultrasound. The magnitude of the photoacoustic signal is proportional to local fluence and the optical absorption coefficient of the illuminated tissue at the wavelength of the laser pulse. Hence, images produced by this method represent optical absorption, a parameter that is independent of the change of ultrasound impedance depicted by ultrasound. For example, the laser wavelength may be tuned to the absorption peaks of oxy- or deoxy-hemoglobin to highlight microvasculature [30] which cannot be obtained with pulse-echo ultrasonic imaging.

Resolution of photoacoustic imaging

The resolution of photoacoustic imaging is affected by both the properties of the light source and the ultrasound transducers used to detect the ultrasound signal. After a pulsed irradiation, the temperature and stress distributions will broaden with time due to thermal diffusion and stress relaxation. The duration of the light pulse must be shorter than the thermal and stress confinement traversal times for a region of the desired resolution dimension. The thermal confinement time is approximately $L^2/4D_T$, where L represents the dimension of the irradiated tissue and D_T represents thermal diffusivity, typically about 1.4×10^{-3} cm^2/sec. Stress confinement time is defined as L/c, where c is the tissue speed of sound. For a resolution of 20

μm, the above relations indicate thermal and stress confinement times of 1 msec and 13 nsec, respectively. From this, it is apparent that stress confinement is the determining parameter and the laser pulse must be no longer than 13 nsec to obtain the required 20-μm resolution. The actual axial and lateral resolution obtained with a photoacoustic imaging system is also limited by the bandwidth and focal properties of the ultrasound transducer used to receive the photoacoustic signal. For an unfocused light source, lateral resolution simply corresponds to the dimension and wavelength of ultrasound, the lateral resolution is given by $1.22 \times F\frac{\lambda}{D}$, where λ is the wavelength of ultrasound, F is the focal length of the transducer and D is the diameter of the transducer. The axial resolution is given by $\frac{f_0 \times \lambda}{4B}$, where f_0 is the center frequency of the transducer, B is the bandwidth of the transducer. For a transducer with 1cm diameter, 3cm focal length, 20-MHz center frequency and 8–MHz bandwidth, the lateral resolution is 270 μm and the axial resolution is 46 microns.

Photoacoustic imaging can provide a better lateral and axial resolution than ultrasound if the laser pulse is focused within the focus of ultrasound and the image is constructed according to the locations of the focused laser beam.

Photoacoustic imaging in the past was done by utilizing intense laser pulses to illuminate a large area and the spatial resolution was determined by the focal properties and frequency of the ultrasound transducer and did not take full advantage of the focusing property of light [31, 32]. Recently, our group in collaboration with Dr. Ronald Silverman of Weill Cornell Medical College has demonstrated photoacoustic imagers that are capable of micron-level resolution.

This section discusses the realization of high-resolution photoacoustic imaging based on a custom-made ring transducer, which allows focused laser and ultrasound beams to be launched collinearly from a compact monolithic device toward a common focus. By focusing the laser

beam to a spot far smaller than achievable with a transducer, the lateral resolution can be significantly improved compared with that obtained with pulse-echo ultrasound or by photoacoustic imaging with an unfocused light source.

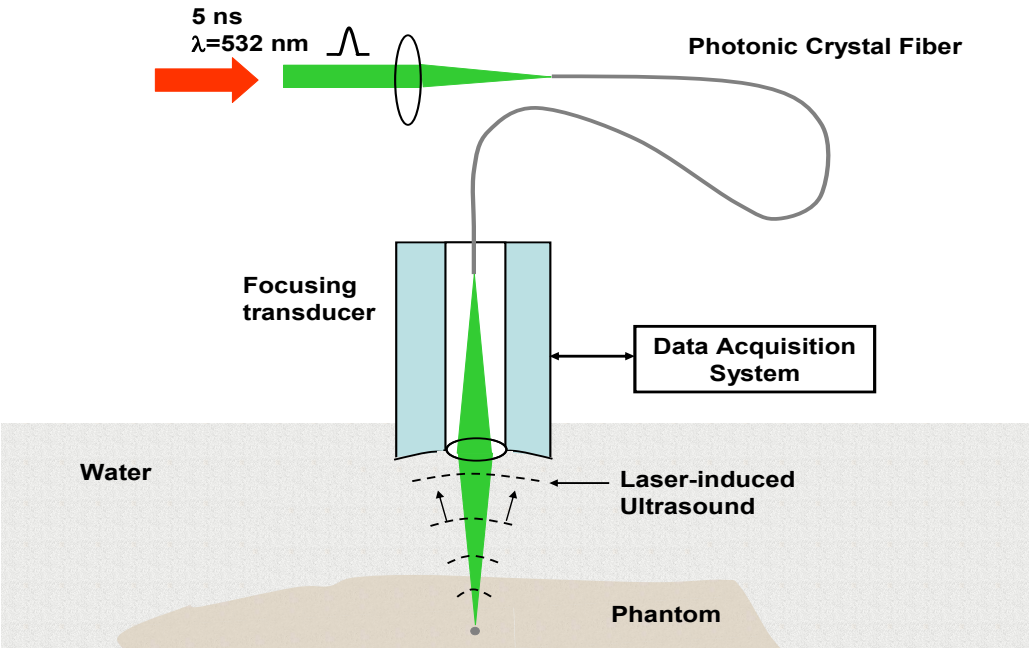

Figure 24. Schematic of the experiment setup for photoacoustic imaging [16]

The experimental setup is shown in Fig. 24. The focusing ring transducer has a diameter of 1 cm with 0.5 cm diameter hole at the center to allow the laser beam to pass through. The acoustic focal length is 3 cm. The center frequency of the transducer is 20 MHz. A passively Q-switched Cr:Nd co-doped yttrium aluminum garnet microchip laser similar to the type described in Chapter 3, is used as the light source. The laser generates 5 ns pulses at a repetition rate of 500 Hz and pulse energy of 10 microjoules at 1064nm. The laser pulse is focused into a Potassium titanyl phosphate (KTP) crystal to generate second-harmonic radiation at 532–nm wavelength.

The conversion efficiency is 50% and the laser beam after the KTP crystal contains equal intensity of 532nm and 1064nm radiation. Either wavelength may be selected by using a bandpass filter. The laser pulses are coupled into a photonic crystal fiber with a core diameter of 20 μm which supports a single transverse mode with a Gaussian modal profile. The laser pulse energy at the tissue is 1 μJ. A combination of time-resolved detection of the photoacoustic waves with linear scanning along the lateral direction generated cross-sectional (B-scan) images. The system can also acquire pulse-echo ultrasound images for the same cross section for comparison. The samples include tissue-mimicking phantoms made of polyvinyl alcohol (PVA) with graphite particles on the surface or distributed within the volume and tissues including the ciliary body from a pig eye.

The lateral and axial resolutions of pulse-echo ultrasound and photoacoustic imaging are compared by examining the cross-sectional (B-scan) images of an aluminum wire in water at the same location. The images are shown in Fig. 25. The lateral full width at half maximum (6dB) width of the ultrasound image shown in Fig. 25(a) is measured to be 170 μm, which is consistent with the theoretical resolution of 180 μm based on the aperture and center frequency of the transducer. The lateral width measured with the photoacoustic imaging, shown in Fig. 25(b), is 35 μm, which is consistent with the wire diameter of 25 μm and the focused spot size of 20 μm. There is also a significant improvement in the axial resolution of the photoacoustic image compared to pulse-echo ultrasound image. The photoacoustic signal caused by thermally induced stress transients is spike-like and shorter than the pulse-echo ultrasound signal. The difference in signal bandwidth is illustrated in the typical oscilloscope traces and spectra shown in Fig. 25. From the 6dB bandwidths of the signals, the axial resolutions for pulse-echo ultrasound and photoacoustic images are 46 and 20 μm, respectively.

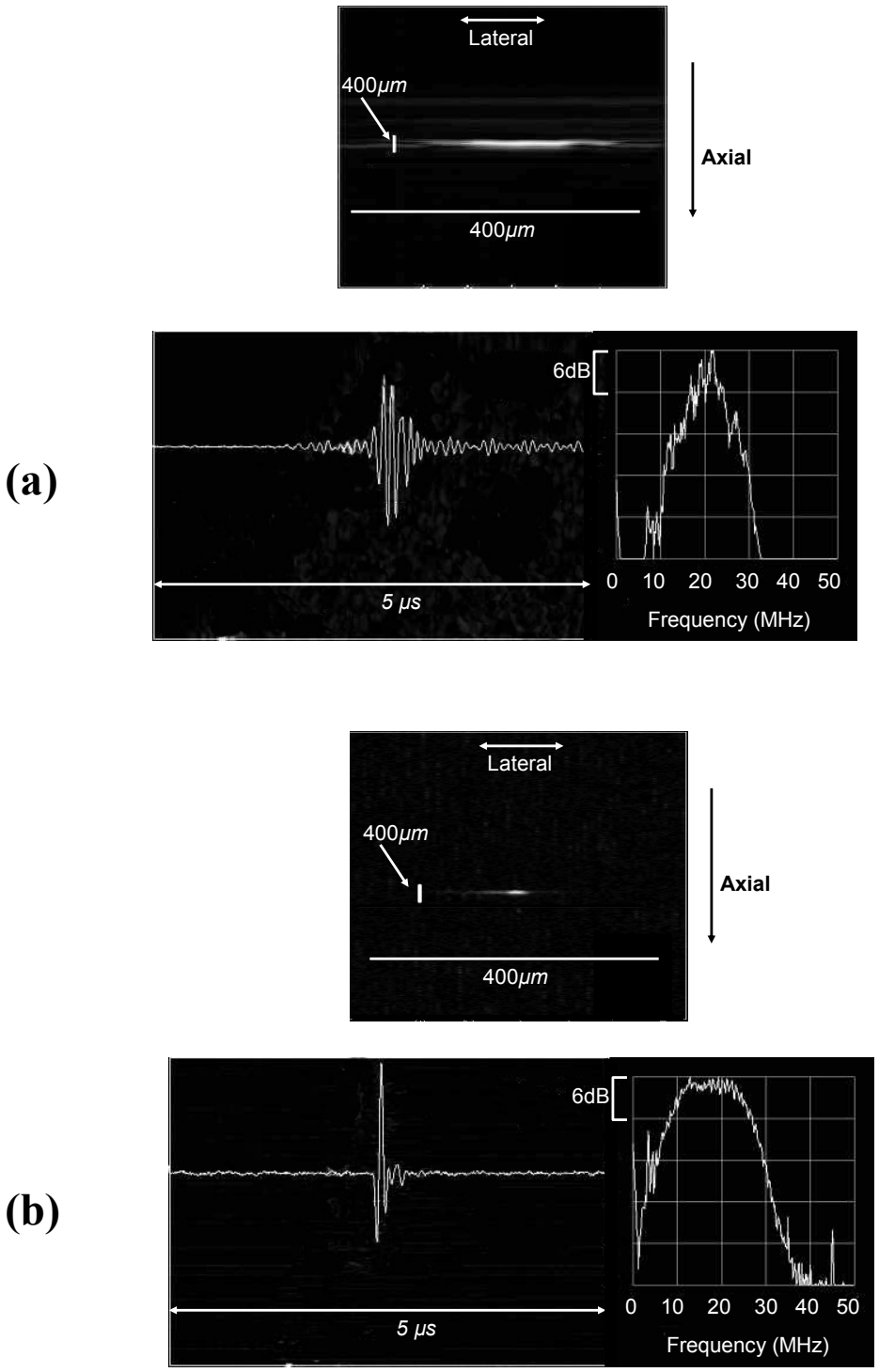

Figure 25. (a) Pulse-echo ultrasound and (b) photoacoustic images of an aluminum wire and corresponding oscilloscope traces and spectra of signals.

Fig. 26 shows the schematic configuration of the two coaxial laser and ultrasound beams. The ultrasound beam has a 270 μm diameter focus focused by a 20MHz-central-frequency transducer with 1 cm diameter and 3 cm focal length. Meanwhile, the Gaussian laser beam is focused within the ultrasound focus to generate the acoustic signal which can be detected by transducer most efficiently. The laser beam has a 20 μm diameter focus and 1.5 mm Rayleigh range which is defined as the distance from a beam waist where the mode radius increased by $\sqrt{2}$. Thus for one B-scan in clear medium, this configuration can provide the same high lateral resolution within 1.5mm depth.

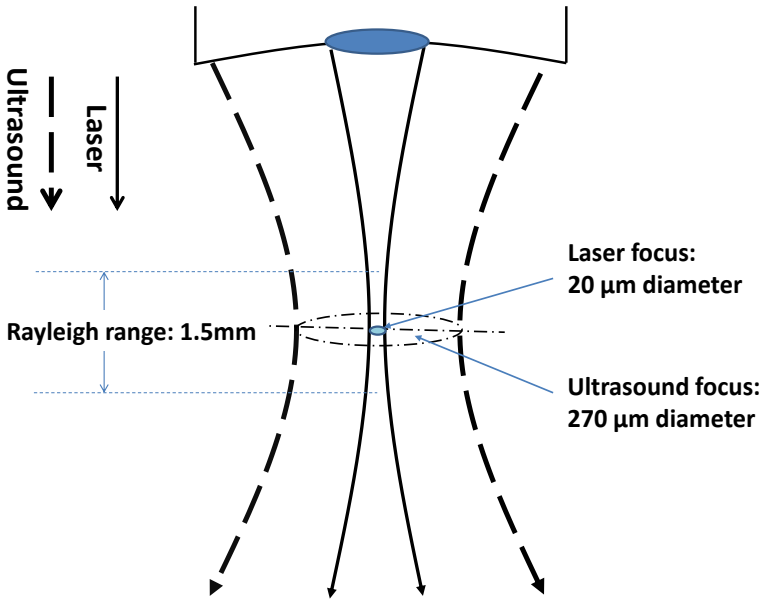

Figure 26. Depth of focus of ultrasound and laser beams.

Fig. 27 shows the ultrasound and corresponding photoacoustic B-scan images of the same cross sections in tissue-mimicking phantoms. The phantoms are made of 10% PVA in water with 25 μm sephadex particles suspended in the phantom to create ultrasound and optical properties equivalent to those in soft tissues. The phantom has no absorption at 532 nm but strong optical scattering is present. The acoustic properties of PVA of the same composition are detailed in Ref 34. We also created phantoms with 8 μm graphite particles, which strongly absorb light, either suspended in the phantom material volumetrically or only on the surface layer.

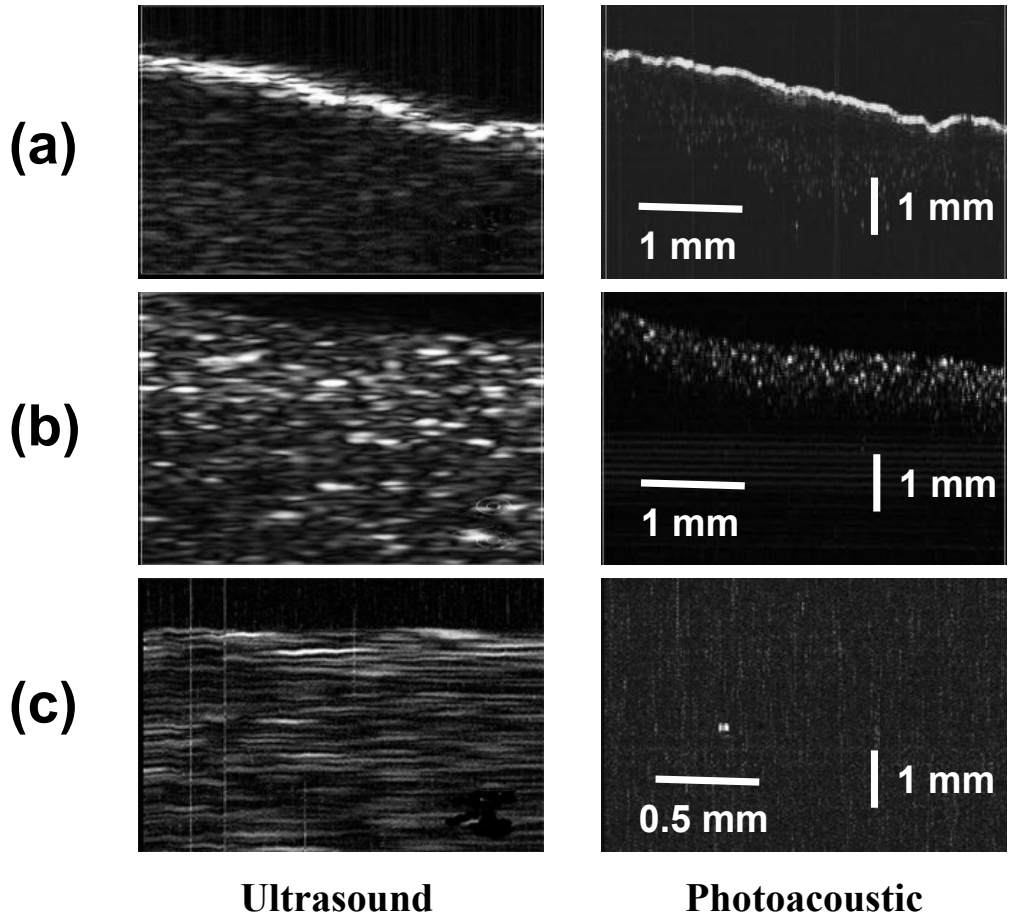

Figure 27. Pulse-echo ultrasound and photoacoustic images of the phantoms with (a) graphite powder on surface, (b) graphite powder uniformly suspended in volume, and (c) 75 μm-diameter human hair embedded in phantom with 2% 25-μm sephadex scatterers.

The images in Fig. 27(a) are scans of graphite particles on the surface of the phantom. The surface features of the phantom are revealed with better clarity and higher resolution with the photoacoustic technique. Both imaging techniques reveal the presence of low-density graphite particles, which diffused into the phantom. The ultrasound signals penetrate deeper into the sample while the photoacoustic signals have limited penetration depth, in this case, approximately 1 mm, once a strong absorbing structure along the line of sight is encountered. The images in Fig. 27(b) are scans of a phantom with 8-micron-diameter graphite particles uniformly suspended throughout the volume. The photoacoustic image shows better clarity and higher resolution of randomly distributed particles. While some signals in the photoacoustic images and their corresponding ultrasound signals are recognizable, the images of optical absorption and discontinuity of acoustic impedance are distinctly different in appearance and the ultrasound does not have the resolution to reveal the true size and shape of the particles. The images in Fig. 27(c) are the cross-sectional views of a 75 μm human hair embedded at 1 mm below the surface of a phantom with 2% 15 μm diameter sephadex scatters suspended throughout the volume. The hair is clearly resolved in the photoacoustic image but not in the ultrasound image presumably due to the small discontinuity in the acoustic impedance of the hair in the phantom and the presence of acoustic scattering from the phantom material itself. Thus the signal from the hair is buried in the strong background. The hair is clearly resolved in the photoacoustic image because hair contains melanin which absorbs light while the surrounding media are transparent. Melanin is present in melanomas which occur in eye and skin. Melanin is also present in other type of pigmented tumors. The ability to detect small objects based on melanin and other light absorbing substances makes photoacoustic a powerful tool in clinical diagnostics.

In optical scattering media such as biological tissues, the focused laser beam will expand due to lateral diffusion as it propagates deeper into the tissues. The advantage of high resolution is expected to hold within the transport mean free path, which, in soft tissues, is about 1 mm [35]. An example of high-resolution image of a real tissue is given in Fig. 28, where the B-scan pulse-echo and photoacoustic images of the ciliary body of a pig eye are presented.

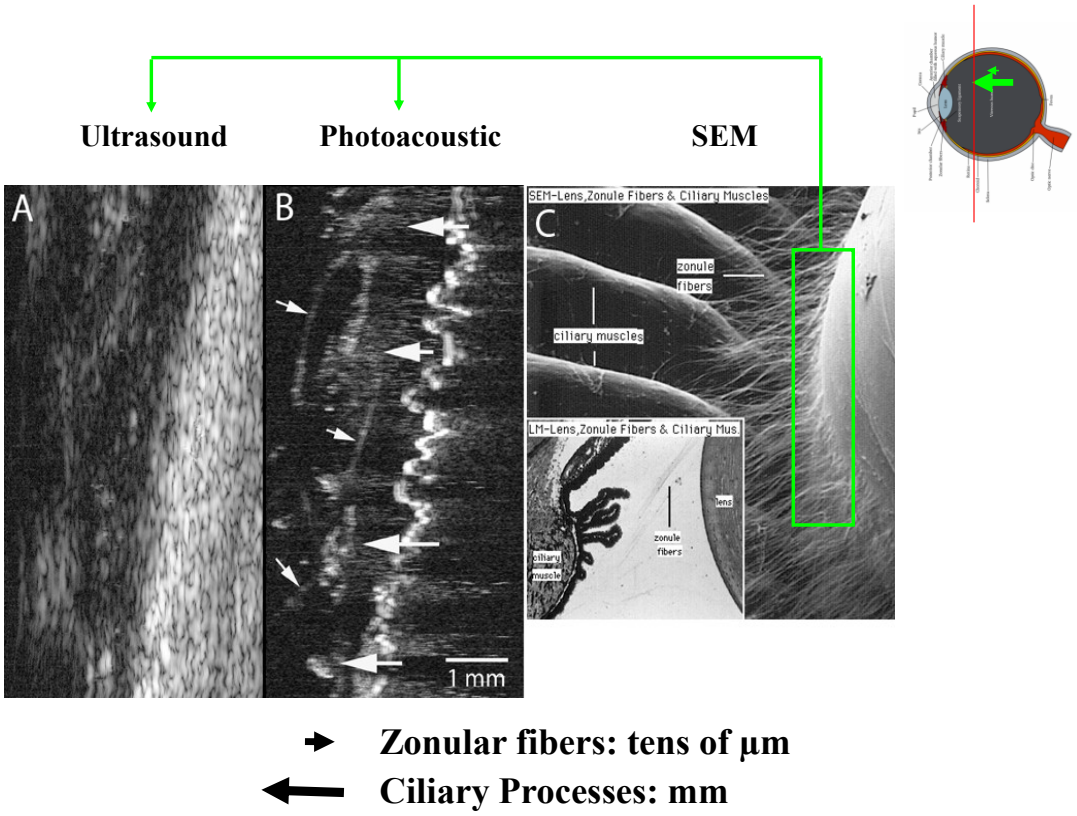

Fig. 28. Pulse-echo, photoacoustic and scanning electron microscopy (SEM)images of the ciliary body of an ex-vivo pig eye

The ciliary body, located underneath the iris, is the tissue that generates fluids to keep the eyeball inflated. The scan is done in a plane perpendicular to the ciliary processes from the back of the

eye after it was cut in half perpendicular to its axis as shown in the inset of Fig. 28. The 20-MHz pulse-echo ultrasound does not produce sufficient structural information other than a hint of the ciliary body and underlining tissue surface. The photoacoustic image, despite the scattering in the tissues, reveals four individual processes, the hair-like zonular fibers of μm diameter and the underlining surface of iris with a 2 mm penetration depth. Also shown in Fig. 28 is the high-resolution image of scanning electron microscope. The electron microscope has much higher resolution, but is not applicable to live patients and animals because the tissue must be taken out of the body and placed in high vacuum for examination. Photoacoustic imaging is noninvasion and has high enough resolution to revel essential features of the tissue.

4.3 Discussion and Conclusion

The current study points to potential applications of photoacoustic imaging in clinical examination of superficial and thin tissues containing optically absorbing chromophore, such as melanin and hemoglobin. The design of the device is particularly suited for imaging of retina and choroids, which are optically accessible through the intervening ocular media (cornea, aqueous, pupil, lens, and vitreous). Because of the 24 mm axial length of a typical eye, the use of ultrasound frequencies above about 20 MHz are impractical due to the strong attenuation in water and the lens. The use of a focused laser will allow at least one-order-of-magnitude improvement in resolution over conventional ultrasound imaging of the retina/choroids.

Photoacoustic imaging is based on absorption of light. Because absorption spectra of the molecular constituents in tissues differ significantly, photoacoustic imaging at multiple wavelengths offers the potential to differentiate molecules of interest. For example, the distinct

absorption spectra of oxy- and deoxyhemoglobin not only allow imaging of vascular structures (due to the presence of blood within them) but also detecting ischemia (insufficient blood flow).

To date, we have conducted photoacoustic imaging in tissues of ex-vivo eye. The ultimate goal of this study is to be able to conduct photoacoustic imaging in the intact eye. We anticipate a number of issues that must be addressed when imaging an intact eye:

1. Diverging paths of light and ultrasound in lens-like media.

The cornea and lens will induce refractive effects on both the ultrasound and laser beams. Although the refractive effect caused by the spherical surface of the cornea is reduced because of the normal saline coupling medium (as opposed to air) at the anterior corneal interface, the beams will still diverge somewhat at the retina. Based on known speed of sound and refractive indices and surface curvatures of the cornea and lens, we have traced the laser and ultrasonic beam paths as they travel through the eye. For focused laser and ultrasonic beams which are incident normally at the center of the pupil and strike the same spot at the retina, these two beams will diverge by 480 μm (laser) and by 900 μm (ultrasound) in opposite directions if they enter the eye at 2.5 mm (the approximate pupil radius) from the center of the pupil. Here we assume that distance from the first surface of the cornea to retina is 2.4 cm. (The divergence will be smaller in animal models where axial length is significantly less.) This effect is illustrated in Fig. 29. The relative displacement is linearly proportional to the beam position from the center. For the non-coaxial case, the laser (entering through the pupil) will exhibit the same displacement. In either case, however, the divergence may exceed the ultrasound beam width, and a compensatory mechanism is needed to ensure the two beams overlap during the scan. A possible approach is to attach the optical fiber to an x-y stage that is independent of the

translation stage used for scanning. At extrema of the lateral scan positions, the x-y stage will perform a search to maximize the photoacoustic signal. During the scan, the x-y stage will adjust fiber position according to a linearly interpolated displacement from the maximum. This method will be applicable for coaxial and non-coaxial probe configurations. Using a 5-μm single-mode optical fiber, sufficient space will be available in the central aperture of the probe to perform required translations.

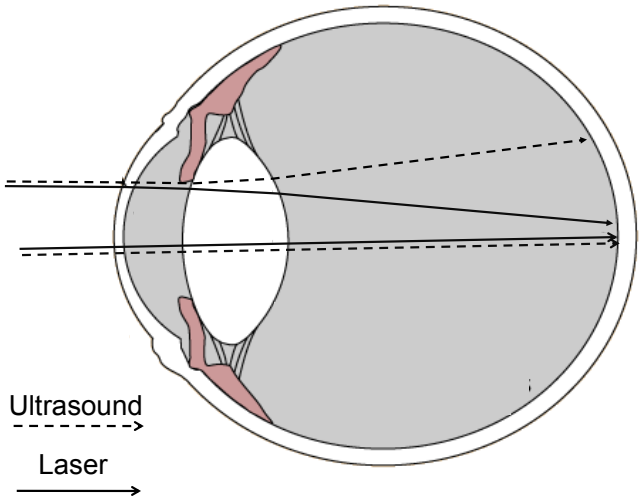

Figure 29. Beam paths of confocal ultrasonic and laser beams entering the eye from the center and edge of pupil.

2. Addressing potential difficulties in imaging the posterior region of the eye

While optically transparent, the intervening structures of the anterior segment (cornea and lens) introduce potential problems for imaging the retina, choroid and optic nerve. The lens is a strong acoustic attenuator and might cause reduced signal-to-noise ratio at higher frequencies (e.g., 20 MHz). Potential solutions include use of lower center frequency ultrasound which

suffers less attenuation in the lens. The use of angled rather than co-axial probes, as shown in Fig.30, may also be helpful. In this case, the ultrasound beam avoids the lens and its refractive and attenuating effects.

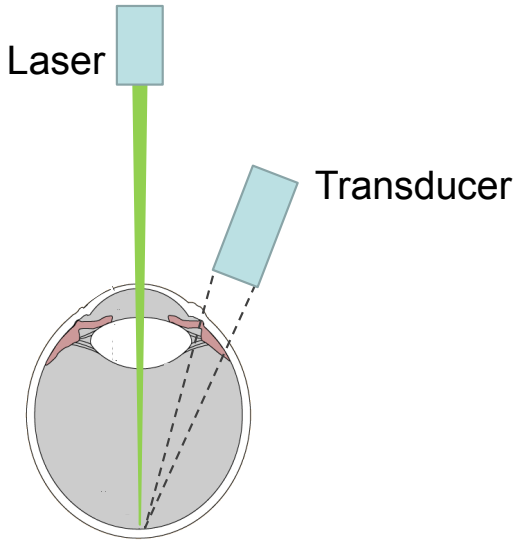

Figure 30. Angled ultrasound and laser beams alignment

3. Conformance with ANSI MPE standards

Safety is a major concern in any ophthalmic application of lasers. The wavelengths used in our experiments, including 532 nm and 1064 nm, fall in the region of retina hazard ranges from 400nm to 1400nm as defined in the American National Standards Institute (ANSI) guidelines [36]. We have calculated the fluence used in our experiments and compared it with the maximum permissible exposure (MPE) published in the ANSI standards. The fluence for safe use of laser depends on the wavelength, duration of exposure, and whether the light is from a point or an

extended light source. In our experiments, the laser beam has a high degree of spatial coherence and must be treated as a point source.

The ANSI standard is based on the assumption that any point light source is treated as being focused by the cornea and lens to an approximately 20 μm diameter spot on the retina. If we assume that areas irradiated by consecutive laser pulses in a rapid scanning photoacoustic system do not overlap, the single-exposure MPE standard is applicable. For a laser beamwidth smaller than the maximum pupil aperture of 7-mm diameter, the energy must be averaged over the pupil area for comparison with the MPE.

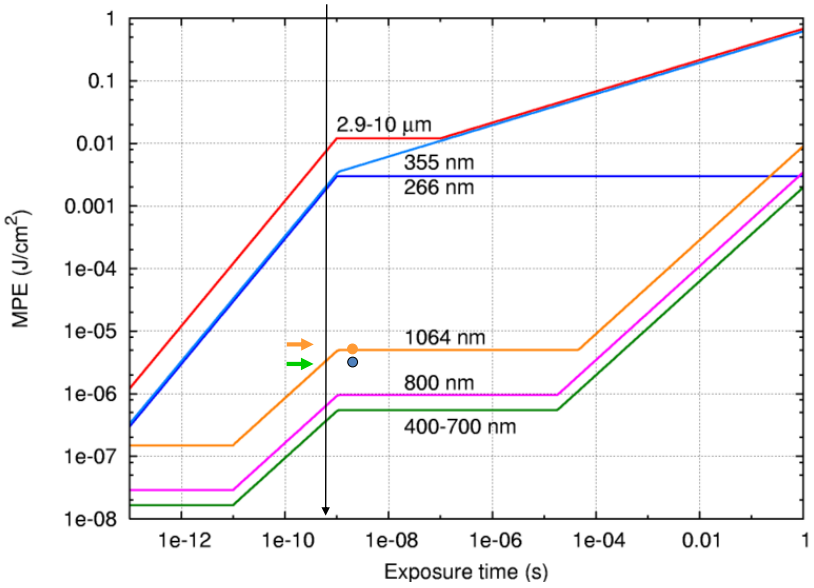

Figure 31. Maximum permissible exposure for various exposure time and wavelengths.[36]

Fig.31 shows the MPE for various exposure time and wavelengths for non-repetitive exposure. The fluence of 1 μJ pulse energy over a dilated pupil of 7 mm diameter is 2.56 μJ/cm^2,

as indicated by the orange and green dots for 1064nm and dot in Fig.31 ,which is a factor of 10 larger than the MPE of 0.25 $\mu J/cm^2$ at 532 nm for a 5-ns pulse and approximately equal to the MPE of 2.5 $\mu J/cm^2$ at 1064 nm. Since the PAI signal, especially at 532 nm, was quite high, the power densities compliant with ophthalmic ANSI standards are likely practicable.

In conclusion, the realization of a high-resolution photoacoustic imager has been demonstrated, which allows microscopy examination of tissues over a long working distance. The system is based on a ring transducer, which allows focused laser and ultrasound beams to be launched from a compact monolithic device. The combination of focused laser beam and short pulse irradiation led to significant improvement in resolution in both the lateral and axial directions compared to the pulse-echo imaging technique.

APPENDIX

List of Publications

Fanting Kong, Y. C. Chen, Harriet O. Lloyd, Ronald H. Silverman, Hyung Ham Kim, Jonathan M. Cannata,and K. Kirk Shung,"High-resolution photoacoustic imaging with focused laser and ultrasonic beams" Appl. Phys. Lett., 94, 033902 (2009).

Fanting Kong, Liping Liu, Yi Zhou, Shou-Huan Zhou , Y.C. Chen, " Phase locking of short-pulse Q-switched lasers" Opt. Commun. 282, 1622 (2009).

Fanting Kong, Liping Liu, Charlotte Sanders, Y. C. Chen, and Kotik K. Lee, " Phase locking of nanosecond pulses in a passively Q-switched two-element fiber laser array", Appl. Phys. Lett., 90, 151110 (2007).

Liping Liu, Yi Zhou, Fanting Kong, Y.C. Chen and K. K. Lee, "Phase locking in fiber laser arrays with varying path length", Appl. Phys. Lett., 85, 4837 (2004).

BIBLIOGRAPHY

[1] Ya-Xian Fan, Fu-Yun Lu, Shu-Ling Hu, Ke-Cheng Lu, Hong-Jie Wang, Xiao-Yi Dong, and Guang-Yin Zhang, "105-kW peak-power double-clad fiber laser", IEEE Photonics Tech. Lett. 15, 652 (2003).

[2] Z. J. Chen, A. B. Grudinin, J. Porta and J. D. Minelly, "Enhanced *Q* switching in double-clad fiber lasers", Opt. Lett. **23**, 454 (1998).

[3] M. Laroche, H. Gilles, S. Girard, N. Passilly, and K. Ait-Ameur, "Nanosecond pulse generation in a passively Q-switched Yb-doped fiber laser by Cr^{4+}:YAG saturable absorber", IEEE Photonics Tech. Lett. **18**, 764 (2006).

[4] Mohammed Salhi, Ammar Hideur, Thierry Chartier, Marc Brunel, Gilles Martel, and Cafer Ozkul, "Evidence of Brillouin scattering in an ytterbium-doped double-clad fiber laser", Opt. Lett. **27**, 1294 (2002).

[5] James R. Leger, "Lateral Mode Control of an AlGaAs Laser Array in a Talbot Cavity", Appl. Phys. Lett. **55** (4)**,** 334 (1989)

[6] M. Wrage, P. Glas, M. Leitner, "Combined phase locking and beam shaping of a multicore fiber laser by structured mirrors", Opt. Lett. 26, 980 (2001).

[7] M.Wrage, P.Glas, D.Fischer, M. Leitner, N. N. Elkin, D. V. Vysotsky, A. P. Napartovich and V. N. Troshchieva, "Phase-locking of a multicore fiber laser by wave propagation through an annular waveguide", Opt. Commun., 205, 367 (2002).

[8] Christopher J. Corcoran, and Frederic Durville, "Experimental demonstration of a phase-locked laser array using a self-Fourier cavity", Appl. Phys. Lett. **86** 201118 (2005).

[9] P. K. Cheo, A. Liu, and G. G. King, "A high-brightness laser beam from a phase-locked multicore Yb-doped fiber laser array", IEEE Photonics Technol. Lett. 13, 439 (2001).

[10] J. Anderegg, S. Brosnan,M. Weber, H. Komine, and M. Wickham, "8-W coherently phased 4-element fiber array, " Proc. SPIE,vol. 4974, pp. 1-6, 2003

[11] Liping Liu, Yi Zhou, Fanting Kong, Y. C. Chen, and Kotik K. Lee, "Phase locking in a fiber laser array with varying path lengths", Appl. Phys. Lett. **85** 4837 (2004).

[12] Yi Zhou, Liping Liu, Candice Etson, Yonatan Abranyos, Angela Padilla, and Y. C. Chen, "Phase locking of a two-dimensional laser array by controlling the far field pattern", Appl. Phys. Lett. **84** 3025 (2004).

[13] Jingwen Xu, K.K. Lee, and Y.C. Chen, "Phase locking in a two-element laser array with detuning" Opt. Commun. 117, 198-126 (1995).

[14] Fanting Kong, Liping Liu, Charlotte Sanders, Y. C. Chen, and Kotik K. Lee, " Phase locking of nanosecond pulses in a passively Q-switched two-element fiber laser array", Appl. Phys. Lett., 90, 151110 (2007).

[15] Fanting Kong, Liping Liu, Yi Zhou, Shou-Huan Zhou , Y.C. Chen, " Phase locking of short-pulse Q-switched lasers" Opt. Commun. 282, 1622 (2009).

[16] Fanting Kong, Y. C. Chen, Harriet O. Lloyd, Ronald H. Silverman, Hyung Ham Kim, Jonathan M. Cannata,and K. Kirk Shung,"High-resolution photoacoustic imaging with focused laser and ultrasonic beams" Appl. Phys. Lett., 94, 033902 (2009).

[17] http://news.thomasnet.com/fullstory/557950

[18] Pask, H.M.; Carman, R.J.; Hanna, D.C.; Tropper, A.C.; Mackechnie, C.J.; Barber, P.R.; Dawes, J.M. **"**Ytterbium-doped silica fiber lasers: versatile sources for the1-1.2 μm region**",** Selected Topics in Quantum Electronics, IEEE Journal of Volume 1, Issue 1, Apr 1995 Page(s):2 – 13

[19] M. Tateda, S. Tanaka, and Y. Sugawara, "Thermal characteristics of phase shift in jacketed optical fibers", Appl. Opt. 19, 770 (1980).

[20] Shouhuan Zhou, K.K. Lee, Y.C. Chen, S. Li, "Monolithic self-Q-switched Cr,Nd:YAG laser", Opt. Lett, 18, 511 (1993).

[21] C. J. Pavlin, K. Harasiewicz, M. D. Sherar, and F. S. Foster, "Clinical use of ultrasound biomicroscopy", Ophthalmology 98, 287 (1991).

[22] F. L. Lizzi, A. Kalisz, M. Aster, D. J. Coleman, R. H. Silverman, and D. Z. Reinstein, "Very-high frequency ultrasonic imaging and spectral assays of the eye", Acoust. Imaging 23, 107 (1997).

[23] S. El-Gammal, K. Hoffman, and T. Auer, in Ultrasound in Dermatology, 1st ed., edited by K. Hoffman (Springer, Germany, 1992), pp. 297-321

[24] C. G. A. Hoelen, F. F. M. de Mul, R. Pongers, and A. Dekker, "Three-dimensional photoacoustic imaging of blood vessels in tissue", Opt. Lett. 23, 648 (1998).

[25] Oraevsky AA, Karabutov AA. Optoacoustic tomography, in Biomedical Photonics Handbook, ed by T. Vo-Dinh, CRC Press, 2003, Vol. PM125, Chapter 34, pp.34/1-34/34.

[26] Oraevsky AA, Jacques SL, Esenaliev RO, Tittel FK. "Laser based optoacoustic imaging in biological tissues", Proc. SPIE 1994;2134A:122-8.

[27] Kruger RA. “Photoacoustic ultrasound”, Med Phys 1994;21:127-31.

[28] Xu M, Wang LV. “Photoacoustic imaging in biomedicine”, Rev Sci Instr. 2006;77:041101-1-21.

[29] Oraevsky AA, Jacques SL, Tittel FK. “Determination of tissue optical properties by time-resolved detection of laser-induced stress waves”, Proc SPIE 1993;1882:86-101.

[30] L. V. Wang, H. F. Zhang, and K. Maslov, Biomedical Optics, Technical Digest (CD) (Optical Society of America, 2006), Paper No. WD1

[31] R. A. Kruger, W. L. Kiser, D. R. Reineche, and G. A. Kruger, “Thermoacoustic computed tomography using a conventional linear transducer array”, Med. Phys. 30, 856 (2003).

[32] S. Manohar, R. G. H Willemink, F. van der Heijden, C. H. Slump, and T. G. vanLeeuwen, “Concomitant speed-of-sound tomography in photoacoustic imaging”, Appl. Phys. Lett. 91,131911 (2007).

[33] K. Maslov, H. F. Zhang, S. Hu, and L. V. Wang, “Optical-resolution photoacoustic microscopy for in vivo imaging of single capillaries”, Opt. Lett. 33, 929-931, (Apr. 2008).

[34] R. G. Holt and R. A. Roy, “Measurements of bubble-enhanced heating from focused, MHz-frequency ultrasound in a tissue-mimicking material”, Ultrasound Med. Biol. 27, 1399 (2001).

[35] H. F. Zhang, K. Maslov, G. Stoica, and L. V. Wang, “Functional photoacoustic microscopy for high-resolution and noninvasive in *vivo* imaging”, Nat. Biotechnol. 24, 848 (2006).

[36] American national standard for safe use of lasers ANSI Z136.1-2007. Orlando; Laser Institute of America, 2007